The Astrophysical Journal, 750:157 (24pp), 2012 May 10 doi:10.1088/0004-637X/750/2/157
© 2012. The American Astronomical Society. All rights reserved. Printed in the U.S.A.

THE NATURE OF TRANSITION CIRCUMSTELLAR DISKS. III. PERSEUS, TAURUS, AND AURIGA*

Lucas A. Cieza[1,5], Matthias R. Schreiber[2], Gisela A. Romero[2,3], Jonathan P. Williams[1],
Alberto Rebassa-Mansergas[2], and Bruno Merín[4]
[1] Institute for Astronomy, University of Hawaii at Manoa, Honolulu, HI 96822, USA; lcieza@ifa.hawaii.edu
[2] Departamento de Fisica y Astronomia, Universidad de Valparaíso, Valparaíso, Chile
[3] Facultad de Ciencias Astronómicas y Geofísicas, UNLP, La Plata, Argentina
[4] Herschel Science Centre, ESAC-ESA, P.O. Box 78, 28691 Villanueva de la Cañada, Madrid, Spain
Received 2011 November 8; accepted 2012 March 19; published 2012 April 25

ABSTRACT

As part of an ongoing program aiming to characterize a large number of *Spitzer*-selected transition disks (disks with reduced levels of near-IR and/or mid-IR excess emission), we have obtained (sub)millimeter wavelength photometry, high-resolution optical spectroscopy, and adaptive optics near-infrared imaging for a sample of 31 transition objects located in the Perseus, Taurus, and Auriga molecular clouds. We use these ground-based data to estimate disk masses, multiplicity, and accretion rates in order to investigate the mechanisms potentially responsible for their inner holes. Following our previous studies in other regions, we combine disk masses, accretion rates, and multiplicity data with other information, such as spectral energy distribution morphology and fractional disk luminosity, to classify the disks as *strong candidates* for the following categories: grain-growth-dominated disks (seven objects), giant planet-forming disks (six objects), photoevaporating disks (seven objects), debris disks (11 objects), and cicumbinary disks (one object, which was also classified as a photoevaporating disk). Combining our sample of 31 transition disks with those from our previous studies results in a sample of 74 transition objects that have been selected, characterized, and classified in a homogenous way. We discuss this combined high-quality sample in the context of the current paradigm of the evolution and dissipation of protoplanetary disks and use its properties to constrain different aspects of the key processes driving their evolution. We find that the age distribution of disks that are likely to harbor recently formed giant planets favors core accretion as the main planet formation mechanism and a ~2–3 Myr formation timescale.

Key words: binaries: general – circumstellar matter – protoplanetary disks – stars: pre-main sequence

Online-only material: color figures

1. INTRODUCTION

Protoplanetary disks evolve through a variety of physical processes. Early in its evolution, a massive gas-rich disk loses mass through accretion onto the star, outflows, and photoevaporation by high-energy photons (Gorti et al. 2009). At the same time, grains grow into larger bodies that settle onto the midplane of the disk where they can grow into rocks, planetesimals, and beyond. Dust settling steepens the slope of the mid- and far-infrared (IR) spectral energy distribution (SED) because a smaller fraction of the stellar radiation is intercepted by circumstellar dust (Dullemond & Dominik 2004). Also, since grain growth is expected to proceed faster in the inner disk, it could result in an inner opacity hole (Dullemond & Dominik 2005). As the disk mass and accretion rate decrease, chromospheric extreme-ultraviolet (EUV) photons start to penetrate the inner disk and EUV-induced photoevaporation becomes important. When the accretion rate drops below the photoevaporation rate, the outer disk is no longer able to resupply the inner disk with material. At this point, the inner disk drains on a viscous timescale (~10^5 yr) and an inner hole is formed (Alexander et al. 2006). Once this inner hole has formed, the EUV photons can reach the inner edge of the disk unimpeded, preventing any material from the outer disk from flowing into the inner hole. This halts accretion and results in the rapid transition between the classical T Tauri star (CTTS) and the weak-line T Tauri star (WTTS) stage. The disk then quickly photoevaporates from the inside out. Once the remaining gas photoevaporates, the small grains are removed by radiation pressure and Poynting–Robertson drag. What is left constitutes the initial conditions of a debris disk: a gas-poor disk with large grains, planetesimals, and/or planets.

This evolutionary path is certainly not unique as some systems such as LkCa 15, DM Tau, and GM Aur seem to have developed sharp cavities due to the dynamical interactions with close (sub)stellar companions or recently formed giant planets while their outer disks are still quite massive (Najita et al. 2007). Even though the broadest aspects of disk evolution summarized above are relatively well established (see Williams & Cieza 2011 for a recent review on protoplanetary disks and their evolution), we are still far from developing a comprehensive disk evolution theory, for which additional observational constraints are much needed. The so-called transition objects (broadly defined as disks with inner opacity holes) are particularly useful *disk evolution laboratories* as they are the systems where the key physical processes mentioned above have the clearest observational signatures. This is so simply because grain growth, photoevaporation, and dynamical clearing all result in reduced levels of near-IR and/or mid-IR excess emission, which is the defining feature of transition objects.

This paper is the third part of a series from an ongoing project aiming to characterize ~100 *Spitzer*-selected transition disks located in nearby star-forming regions. This coordinated project has two main goals: (1) provide observational constraints on the evolution of primordial disks, their dissipation, and the

---

* Based in part on observations made with the CFHT, under programs 09BH48, 09BH10, 10AH06, and 10BH97.

[5] *Sagan* Fellow.

primordial to debris disk transition, and (2) identify systems with strong evidence for ongoing giant planet formation so they can eventually be used as *planet formation laboratories*. In the first paper of the series (Cieza et al. 2010, hereafter Paper I), we studied a sample of 26 Ophiuchus transition disks, while in the second paper (Romero et al. 2012, hereafter Paper II) we analyzed a sample of 17 objects from the Lupus, Corona Australis, and Scorpius regions. In Papers I and II, we showed that transition disks are a very heterogenous group of objects with disk masses ranging from $<0.6\,M_{\rm JUP}$ to $40\,M_{\rm JUP}$, accretion rates ranging from $<10^{-11}$ to $10^{-7}\,M_\odot\,{\rm yr}^{-1}$, and fractional disk luminosities, L_D/L_*, ranging from a few percent to $\lesssim 10^{-4}$. We also showed that their diverse properties can be understood in terms of different disk evolution processes and distinct evolutionary stages.

Here we present millimeter wavelength photometry (from the Submillimeter Array, SMA, and James Clerk Maxwell Telescope, JCMT), high-resolution optical spectroscopy (from the Canada–France–Hawaii Telescope, CFHT), and adaptive optics (AO) near-infrared imaging (from the Gemini telescope) for 31 *Spitzer*-selected transition circumstellar disks located in the Perseus, Taurus, and Auriga molecular clouds. As in our previous studies, we use these new ground-based data to estimate disk masses, accretion rates, and multiplicity for our sample in order to investigate the mechanisms potentially responsible for their inner opacity holes. These new 31 objects take our total sample of well-characterized transition disks to 74. The structure of this paper is as follows. Our sample selection criteria are presented in Section 2, while our observations and data reduction techniques are described in Section 3. We present our results on disk masses, accretion rates, and multiplicity in Section 4. In Section 5, we discuss the likely origins of the inner holes of the 31 new individual targets and discuss the properties of our combined sample of 74 transition objects in a broader context of disk evolution. Finally, a summary of our results and conclusions is presented in Section 6.

2. SAMPLE SELECTION

We drew our sample from the *Spitzer* catalogs of three northern clouds mapped by three different Legacy Programs: *Cores to Disks* (Perseus molecular cloud[6]), *Taurus* (Taurus molecular cloud[7]), and *Gould's Belt* (Auriga molecular cloud). For a description of the *Cores to Disks* data products, see Evans et al.[8] The *Taurus* catalogs are discussed by Padgett et al.[9] At the time of this writing, the *Gould's Belt* data products have not yet been delivered to NASA's Infra-Red Science Archive (IRSA), but they should also eventually become publicly available through IRSA. As in Papers I and II, we selected all the targets meeting the following criteria:

1. Have *Spitzer* colors [3.6]–[4.5] < 0.25. These are objects with small or no near-IR excess (see Figure 1). The lack of a [3.6]–[4.5] color excess in our targets is inconsistent with an optically thick disk extending inward to the dust sublimation radius and therefore implies the presence of an inner opacity hole. The presence of this inner opacity hole is the defining feature we intend to capture in our sample.

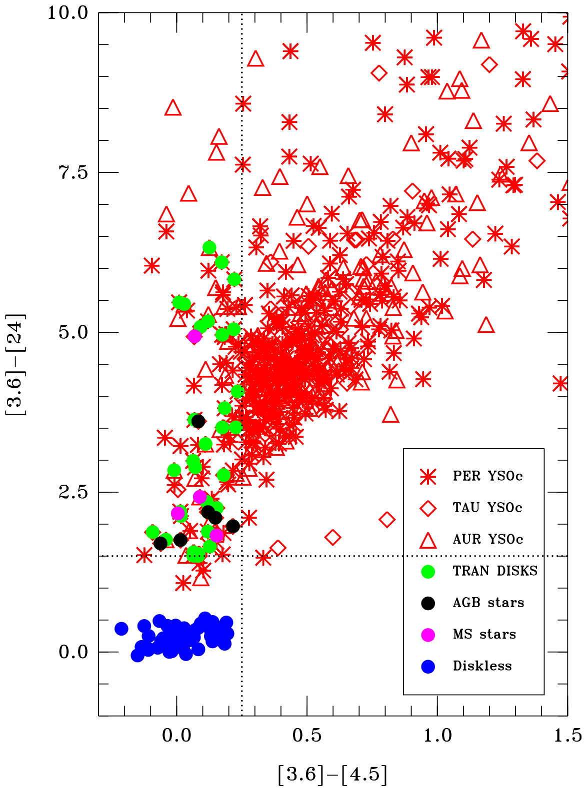

Figure 1. Color–color diagram illustrating our key target selection criteria. Objects with [3.6]–[4.5] < 0.25 and [3.6]–[24] < 0.5 are consistent with bare stellar photospheres. Blue dots are diskless WTTSs from Cieza et al. (2007) used to define this region of the diagram. Red stars and triangles are all the young stellar object candidates (YSOc) in the Perseus and Auriga catalogs from the *c2d* and *Gould Belt* Legacy Projects. Since the catalogs from the *Taurus* project do not provide a YSOc classification, we simply plot all the targets with IR excesses and 3.6 and 24 μm fluxes at least as large as those of the faintest transition disks in our sample (red diamonds). Most PMS stars either are diskless or have excesses at both 4.5 and 24 μm. Our 31 transition disks, shown as green dots, have significant ($>5\sigma$) excess at 24 μm and little or no excess at 4.5 μm, as expected for disks with inner holes.

(A color version of this figure is available in the online journal.)

2. Have *Spitzer* colors [3.6]–[24] > 1.5. We apply this criterion to ensure that all our targets have very significant 24 μm excesses ($>5\sigma$–10σ), unambiguously indicating the presence of circumstellar material. The exact color cut is somewhat arbitrary. We have empirically found that most young stellar object candidates (YSOc) with low 24 μm excesses ([3.6]–[24] $\lesssim$ 1.5) are in fact background asymptotic giant branch (AGB) stars (see Paper II).
3. Are detected with a signal-to-noise ratio >7 in all Two Micron All Sky Survey (2MASS) and Infrared Array Camera (IRAC) wavelengths, as well as at 24 μm, to ensure that we only include targets with very reliable photometry.
4. Have $K_S < 11$ mag, driven by the sensitivity of our near-IR AO observations and to ensure a negligible extragalactic contamination (Padgett et al. 2008).
5. Are brighter than $R = 18$ mag according to the USNO-B1 catalog (Monet et al. 2003), driven by the sensitivity of our optical spectroscopy observations.

The first two selection criteria ([3.6]–[4.5] < 0.25 and [3.6]–[24] > 1.5) effectively become our working definition for a transition disk. These criteria are fairly inclusive and encompass most of the transition disk definitions found in the literature as they select disks with a significant flux decrement

---

[6] Available through IRSA at http://irsa.ipac.caltech.edu/data/SPITZER/C2D/

[7] Available through IRSA at http://irsa.ipac.caltech.edu/data/SPITZER/Taurus/

[8] Available at http://irsa.ipac.caltech.edu/data/SPITZER/C2D/doc/c2d_del_document.pdf

[9] Available at http://irsa.ipac.caltech.edu/data/SPITZER/Taurus/docs/delivery_doc2.pdf

relative to "normal disks" in the near-IR or at all wavelengths. In particular, our definition includes objects with falling mid-IR SEDs such as anemic (Lada et al. 2006) or homologously depleted transition disks (Currie et al. 2009), as well as objects with rising mid-IR SEDs such as classical transition disks (Muzerolle et al. 2010) or cold disks (Brown et al. 2007; Merín et al. 2010). The one type of transition disk that is likely to be underrepresented in our sample is the so-called pre-transitional disk category, which describes systems with optically thin gaps separating optically thick inner and outer disk components (Espaillat et al. 2007). These rare objects tend to have large near-IR excesses that could be excluded by our [3.6]–[4.5] < 0.25 criterion. For a concise description of the complex transition disk nomenclature, see Evans et al. (2009). We find 41 targets that meet all of our selection criteria: 18 objects in Perseus (∼44%), 6 in Auriga (∼15%), and 17 in Taurus (∼41%). We have observed all 41 objects in our target list; however, as discussed in Section 4.1, this list includes six AGB stars and four likely debris disks around main-sequence (MS) stars. The remaining 31 targets are bona fide young stellar objects (YSOs) with circumstellar disks and constitute our science sample. The 2MASS IDs and alternative names, 2MASS and *Spitzer* fluxes, and the USNO-B1 R-band magnitudes for all our 41 targets are listed in Table 1.

The *Spitzer* data of our Perseus transition disks have been presented by Jørgensen et al. (2006) and Rebull et al. (2007). Similarly, the parent sample of our Taurus objects has been discussed by Rebull et al. (2010) and Luhman et al. (2010). We note that while Rebull et al. only used the catalogs from the Taurus Legacy Program as we do, the study by Luhman et al. includes many additional observations of the Taurus region from several General Observer and Guaranteed Time Observations programs. Some well-known Taurus transition disks included in Luhman et al. (e.g., DM Tau and CoKu Tau/4) were not observed as part of the Taurus Legacy Program and therefore are not included in our sample. The *Spitzer* data for the parent population of our Auriga targets have not been published at the time of this writing.

3. OBSERVATIONS

3.1. Optical Spectroscopy

We obtained Echelle spectroscopy for our entire sample using the ESPaDonS Echelle spectrograph on the 3.5 m CFHT at Mauna Kea Observatory in Hawaii. The observations were performed in service mode over four semesters (2009A, 2009B, 2010A, and 2010B). The spectra were obtained in the standard "star+sky" mode, which delivers the complete optical spectra between 3500 Å and 10500 Å at a resolution of 68,000, or 4.4 km s^{-1}. For each object, we obtained a set of three spectra with exposure times ranging from 2.5 to 30 minutes each, depending on the brightness of the target. The data were reduced through the standard CFHT pipeline Upena, which is based on the reduction package Libre-ESpRIT.[10] In Section 4, we use these data to derive the spectral types and accretion rates of our targets.

3.2. Adaptive Optics Imaging

High spatial resolution near-IR observations of our entire sample were obtained in service mode during the 2009B semester with the 8.1 m Gemini North telescope in Mauna Kea using the Near InfraRed Imager and Spectrometer (NIRI) and the Altair AO system. We used the Natural Guide Star mode for the targets brighter than $R = 15.5$ mag and the Laser Guide Star mode for the objects fainter than $R = 15.5$ mag. In all cases, the science target was used as the tip/tilt guide star. J- and K-band observations were obtained with the $f/32$ camera (0.022 arcsec pixel^{-1}, $22'' \times 22''$ field of view). The brightest objects required narrowband filters. For each target, we took five dithered images in each filter with individual exposure times ranging from 1 to 20 s.

The K-band AO images are the most stable and provide the highest Strehl (∼40%) and thus allow the detection of binaries with large brightness ratios. The J-band images provide a point-spread function (PSF) core with a smaller FWHM ($\sim 0\farcs05$) and are better suitable for the detection of very tight systems. The data were reduced with Image Reduction and Analysis Facility using the NIREDUCE task in the NIRI package. In Section 4.4, we use these AO imaging data to constrain the multiplicity of our targets.

3.3. (Sub)millimeter Wavelength Photometry

The (sub)millimeter wavelength photometry is the most expensive component of our observing program in terms of observing time, preventing us from obtaining such data for the entire sample. Two of our targets, 2 (MBO 22) and 26 (FW Tau), have already been detected at (sub)millimeter wavelengths (Merín et al. 2010; Andrews & Williams 2005), while stringent upper limits exist for 33 (ZZ Tau; Andrews & Williams 2005). We also found 850 μm SMA (Ho et al. 2004) archival data for object 9. We have observed 26 of the remaining 37 objects with the SMA. We also obtained Common-User Bolometer Array-2 (SCUBA-2) data using the JCMT for 5 of the 11 targets that were not observed with the SMA. Six objects remain unobserved at (sub)millimeter wavelengths. However, since our (sub)millimeter observing programs gave the lowest priority to objects with little 24 μm excesses and/or lacking accretion signatures, these six unobserved targets turned out to be either an AGB star contaminating our sample (one object) or a debris disk candidate (five objects; see Section 4.1). We note that debris disks are not expected to be detectable at the sensitivity levels of our (sub)millimeter wavelength survey, $M_{\mathrm{dust}} \sim 6$–$15\, M_{\oplus}$ (corresponding to $\sim$2–5 M_{JUP} for primordial disks with a gas-to-dust mass ratio of 100). In fact, this dust mass level is an order of magnitude higher than that of the most massive debris disks observed (Wyatt 2008). None of our conclusions are thus likely to be affected by the lack of a complete millimeter wavelength data set.

3.3.1. Submillimeter Array Observations

Our SMA observations were conducted in service mode, during the 2008B, 2009B, and 2010B semesters. Virtually all the observations were obtained in the compact configuration and with the 230 GHz/1300 μm receiver. The only exception was object 31, which was observed in the extended configuration using the 345 GHz/850 μm receiver. Both the upper and lower sideband data were used, resulting in a total bandwidth of 4 GHz.

Typical zenith opacities during our 230 GHz observations were $\tau_{225\,\mathrm{GHz}} \sim 0.15$–0.25. The 345 GHz extended configuration observations were obtained under significantly better conditions ($\tau_{225\,\mathrm{GHz}} \sim 0.07$). For each target, the observations cycled between the target and two gain calibrators (either 3c111 and 3c84 or 0336+323 and 0449+113), with 20–30 minutes on

---

[10] http://www.cfht.hawaii.edu/Instruments/Spectroscopy/Espadons/Espadons_esprit.html

Table 1
Transition Disk Sample

No.	2MASS ID	Alter. Name	R (mag)	J[a] (mJy)	H (mJy)	K_S (mJy)	$F_{3.6}$[a] (mJy)	$F_{4.5}$ (mJy)	$F_{5.8}$ (mJy)	$F_{8.0}$ (mJy)	F_{24} (mJy)	F_{70}[b] (mJy)	Region
1	03292681+3126475	MBO 15	12.37	7.41e+01	1.03e+02	8.96e+01	4.72e+01	3.20e+01	2.33e+01	1.70e+01	1.89e+01	<8.06e+01	PER
2	03292925+3118347	MBO 22	16.56	1.47e+01	2.89e+01	2.75e+01	1.36e+01	1.02e+01	7.62e+00	6.94e+00	9.52e+01	2.91e+02	PER
3	03302409+3114043	[EDJ2009] 261	17.30	6.83e+00	7.73e+00	6.93e+00	4.99e+00	3.96e+00	3.80e+00	5.04e+00	5.43e+00	<1.05e+01	PER
4	03335108+3112278	[EDJ2009] 300	16.72	4.15e+01	6.37e+01	5.87e+01	3.50e+01	2.50e+01	1.72e+01	1.07e+01	5.06e+00	<1.53e+01	PER
5	03344987+3115498	[EDJ2009] 303	13.79	8.34e+01	1.18e+02	1.04e+02	6.71e+01	4.57e+01	3.44e+01	3.43e+01	4.86e+01	4.04e+01	PER
6	03411412+3159462	[EDJ2009] 307	12.59	1.57e+02	1.37e+02	1.06e+02	5.00e+01	3.24e+01	2.34e+01	1.85e+01	9.64e+00	<6.53e+01	PER
7	03413918+3136106	BD+31 634	10.00	2.37e+02	1.68e+02	1.16e+02	5.05e+01	3.61e+01	2.99e+01	5.26e+01	1.51e+02	<5.75e+01	PER
8	03422333+3157426	[EDJ2009] 323	12.23	1.60e+02	1.39e+02	1.07e+02	5.22e+01	3.39e+01	2.50e+01	2.19e+01	9.45e+00	<2.61e+01	PER
9	03434461+3208177	Cl* IC 348 LRL 67	14.65	2.41e+01	3.61e+01	3.21e+01	1.90e+01	1.49e+01	1.14e+01	1.09e+01	1.04e+02	1.73e+02	PER
10	03440915+3207093	Cl* IC 348 LRL 8	9.41	4.55e+02	3.24e+02	2.39e+02	9.79e+01	6.64e+01	4.63e+01	3.68e+01	1.00e+01	<1.44e+02	PER
11	03441912+3209313	Cl* IC 348 LRL 30	11.24	1.37e+02	1.18e+02	8.32e+01	3.24e+01	2.33e+01	1.60e+01	9.81e+00	3.78e+00	<3.02e+02	PER
12	03442156+3215098	Cl* IC 348 LRL 185	…	1.01e+01	1.31e+01	1.15e+01	5.66e+00	4.29e+00	3.04e+00	1.99e+00	4.84e+00	<1.71e+02	PER
13	03442257+3201536	Cl* IC 348 LRL 72	15.93	2.26e+01	3.55e+01	3.23e+01	1.72e+01	1.11e+01	8.91e+00	7.55e+00	6.76e+01	<7.36e+02	PER
14	03443200+3211439	Cl* IC 348 LRL 12B	12.88	1.49e+02	1.84e+02	1.80e+02	1.38e+02	1.08e+02	2.61e+02	7.66e+02	3.68e+02	<8.65e+02	PER
15	03443694+3206453	Cl* IC 348 LRL 6	11.69	3.31e+02	4.13e+02	3.52e+02	2.08e+02	1.48e+02	1.16e+02	9.26e+01	4.61e+01	<5.38e+02	PER
16	03444351+3207427	Cl* IC 348 LRL 52	17.01	2.27e+01	4.53e+01	4.54e+01	2.68e+01	1.83e+01	1.26e+01	8.65e+00	9.77e+00	<6.80e+02	PER
17	03445614+3209152	Cl* IC 348 LRL 21	14.81	6.21e+01	1.03e+02	1.08e+02	8.69e+01	6.53e+01	5.53e+01	4.38e+01	2.14e+02	<2.30e+02	PER
18	03450142+3205017	Cl* IC 348 LRL 25	12.38	1.19e+02	1.13e+02	9.24e+01	4.36e+01	3.01e+01	2.04e+01	1.36e+01	4.44e+00	<8.10e+01	PER
19	04104210+3805598	BD+37 887	8.47	1.41e+03	1.10e+03	7.76e+02	3.41e+02	2.10e+02	1.51e+02	8.71e+01	4.39e+01	<5.77e+01	AUR
20	04190110+2819420	[GBA2007] 527	16.50	9.81e+01	1.48e+02	1.49e+02	8.79e+01	6.12e+01	4.42e+01	3.19e+01	2.43e+02	4.10e+02	TAU
21	04192625+2826142	V819 Tau	12.01	2.52e+02	3.56e+02	2.85e+02	1.47e+02	8.64e+01	6.58e+01	3.82e+01	2.11e+01	<3.35e+01	TAU
22	04210934+2750368	…	15.55	5.14e+01	5.59e+01	4.79e+01	2.90e+01	2.19e+01	1.66e+01	1.32e+01	9.46e+00	<2.25e+01	TAU
23	04242321+2650084	…	14.48	7.57e+01	1.00e+02	8.94e+01	4.61e+01	3.13e+01	2.24e+01	1.33e+01	4.95e+00	<3.23e+01	TAU
24	04284263+2714039	WDS J04287+2714AB	16.81	2.29e+01	3.83e+01	4.39e+01	3.50e+01	2.76e+01	2.39e+01	1.89e+01	2.27e+01	<2.29e+01	TAU
25	04292083+2742074	IRAS 04262+2735	15.54	6.06e+02	1.06e+03	1.04e+03	6.04e+02	4.17e+02	3.69e+02	5.95e+02	4.28e+02	<2.63e+01	TAU
26	04292971+2616532	FW Tau	14.65	1.16e+02	1.38e+02	1.17e+02	6.48e+01	4.48e+01	3.24e+01	1.80e+01	6.79e+00	<2.35e+01	TAU
27	04295531+2258579	IRAS 04269+2252	13.13	4.41e+03	8.11e+03	8.64e+03	2.70e+03	1.93e+03	1.82e+03	1.45e+03	5.17e+02	<1.94e+01	TAU
28	04300113+3517247	HBC 390	15.51	7.47e+01	1.37e+02	1.30e+02	7.57e+01	4.80e+01	3.08e+01	2.29e+01	2.65e+01	<1.43e+03	AUR
29	04300424+3522238	…	16.53	8.21e+00	1.30e+01	1.13e+01	6.47e+00	4.25e+00	3.23e+00	2.69e+00	2.48e+01	<3.54e+02	AUR
30	04301644+3525217	[HAD2004] LDN 1482 G	12.58	9.60e+01	8.15e+01	6.20e+01	2.78e+01	1.93e+01	1.33e+01	1.00e+01	6.63e+00	<9.85e+01	AUR
31	04303235+3536133	…	15.94	3.13e+01	6.07e+01	6.08e+01	3.37e+01	2.42e+01	1.72e+01	1.55e+01	2.92e+02	<9.60e+01	AUR
32	04304004+3542101	…	15.76	1.83e+01	2.73e+01	2.49e+01	1.44e+01	1.02e+01	7.32e+00	5.57e+00	7.36e+00	<4.46e+01	AUR
33	04305137+2442222	ZZ Tau	13.31	2.54e+02	3.41e+02	2.80e+02	1.65e+02	1.24e+02	1.00e+02	1.09e+02	1.07e+02	<9.50e+01	TAU
34	04312113+2658422	IRAS 04282+2652	14.76	3.14e+03	6.25e+03	7.24e+03	2.46e+03	1.92e+03	2.03e+03	1.29e+03	3.84e+02	<3.00e+01	TAU
35	04314503+2859081	…	13.32	4.14e+01	3.52e+01	2.68e+01	1.16e+01	7.45e+00	4.89e+00	3.03e+00	2.18e+00	<1.54e+01	TAU
36	04330422+2921499	BD+29 719	9.96	7.02e+02	5.50e+02	3.93e+02	1.79e+02	1.22e+02	8.49e+01	8.72e+01	4.31e+02	<3.22e+02	TAU
37	04343549+2644062	…	13.90	5.22e+02	1.11e+03	1.17e+03	6.57e+02	3.97e+02	3.02e+02	2.09e+02	8.01e+01	<1.28e+01	TAU
38	04364912+2412588	HD 283759	10.01	5.27e+02	4.32e+02	3.09e+02	1.12e+02	8.25e+01	5.50e+01	3.36e+01	1.53e+01	2.80e+02	TAU
39	04372486+2709195	HD 283751	11.25	1.94e+02	1.55e+02	1.27e+02	4.65e+01	3.41e+01	2.70e+01	2.07e+01	8.21e+00	<2.37e+01	TAU
40	04385827+2631084	Elia 3-14	15.60	2.73e+02	8.58e+02	1.16e+03	7.48e+02	4.85e+02	3.82e+02	2.42e+02	9.58e+01	<3.24e+01	TAU
41	04403979+2519061	WDS J04407+2519AB	17.87	2.98e+01	4.94e+01	5.36e+01	3.27e+01	2.41e+01	1.63e+01	9.49e+00	6.64e+00	<3.41e+01	TAU

Notes.

[a] All the 2MASS, IRAC, and 24 μm detections are $\geqslant 7\sigma$ (i.e., the photometric uncertainties are $\lesssim 15\%$).

[b] $\geqslant 5\sigma$ detections or 5σ upper limits.

Table 2
Observed Properties

No.	R.A. (J2000) (deg)	Decl. (J2000) (deg)	SpT.	Hα[a] (km s^{-1})	λ_{mm} (mm)	Flux$_{\mathrm{mm}}$[b] (mJy)	σFlux$_{\mathrm{mm}}$ (mJy)	Separ (arcsec)	Pos. Ang. (deg)	ΔK[c] (mag)
1	52.3617	31.4465	M2	140	1.30	<2.9	...	0.25; 1.7	188; 63	0.83; 2.09
2	52.3720	31.3096	M0	280	1.30	6.3	1.1	...	...	>1.65; 3.85
3	52.6003	31.2345	M2	340	1.30	<3.0	...	...	...	>1.82; 3.70
4	53.4628	31.2077	M3	170	1.30	<2.9	...	0.96	101	2.08
5	53.7077	31.2640	M2	450	1.30	6.0	1.2	0.85	231	2.62
6	55.3088	31.9962	A3	−1	0.85	<15.0	...	...	...	>2.95; 5.23
7	55.4132	31.6030	A5	−1	1.30	<3.0	...	...	...	>2.62; 4.86
8	55.5972	31.9619	A0	−1	0.85	<15.0	...	...	...	>3.08; 4.73
9	55.9359	32.1383	M1	280	0.85	31	6.0	...	...	>1.91; 4.01
10	56.0382	32.1192	A2	−1	...	...	...	...	...	>2.64; 4.33
11	56.0797	32.1587	F0	−1	...	...	...	...	...	>2.77; 4.49
12	56.0899	32.2527	M2	130	1.30	<3.0	...	...	...	>0.95; 3.14
13	56.0941	32.0316	M2	140	1.30	<1.5	...	...	...	>1.23; 3.03
14	56.1335	32.1955	A5	−1	1.30	<2.8	...	1.31	274	0.20
15	56.1540	32.1126	G2	−1	1.30	<2.9	...	0.56	207	1.12
16	56.1814	32.1285	M1	150	1.30	<2.5	...	...	...	>1.67; 2.25
17	56.2339	32.1542	K0	360	1.30	<1.1	...	...	...	>2.15; 3.61
18	56.2559	32.0838	A3	−1	...	...	...	0.65	271	2.89
19	62.6755	38.1000	A3	−1	1.30	<3.9	...	...	...	>2.65; 4.59
20	64.7546	28.3284	M6	210	1.30	<3.3	...	...	...	>1.94; 3.94
21	64.8594	28.4373	K7	180	1.30	<5.4	...	...	...	>2.74; 4.03
22	65.2889	27.8436	M4	280	1.30	<3.0	...	0.77	230	1.28
23	66.0967	26.8357	M2	200	...	...	...	...	...	>1.93; 3.19
24	67.1776	27.2344	M4	300	1.30	<3.0	...	0.64	10	0.94
25	67.3368	27.7021	AGB	−1	...	...	...	...	...	>2.27: 3.72
26	67.3738	26.2814	M5	190	0.85	4.5	1.1	0.05	45	∼0
27	67.4805	22.9828	AGB	−1	1.30	<6.0	...	...	...	>3.23; 3.99
28	67.5048	35.2902	K7	370	1.30	<3.3	...	1.3	24	1.01
29	67.5177	35.3733	M0	370	1.30	9.7	1.5	...	...	>2.12; 3.67
30	67.5685	35.4227	A4	−1	1.30	<3.3	...	...	...	>2.41; 4.29
31	67.6348	35.6037	K7	350	0.85	10.0	2.0	0.83	61	2.30
32	67.6669	35.7029	K7	310	1.30	<2.5	...	1.2	307	∼1
33	67.7141	24.7062	M3	330	0.85	<8.0	...	0.07	315	∼0
34	67.8381	26.9784	AGB	−1	1.30	<5.0	...	...	...	>1.69; 2.66
35	67.9377	28.9856	F5	−1	...	...	...	...	...	>3.41; 4.94
36	68.2676	29.3639	B9	−1	1.30	<2.8	...	...	...	>2.07; 3.88
37	68.6479	26.7351	AGB	−1	0.85	<30.0	...	...	...	>2.06; 4.33
38	69.2047	24.2163	F2	−1	0.85	<27.0	...	...	...	>2.73; 3.96
39	69.3536	27.1554	AGB	−1	1.30	<3.3	...	...	...	>3.11; 5.41
40	69.7428	26.5190	AGB	−1	0.85	<30.0	...	...	...	>1.80; 3.66
41	70.1658	25.3184	M5	130	1.30	<2.9	...	...	...	>1.74; 2.34

Notes.
[a] "−1" implies that Hα is seen in absorption.
[b] $\geqslant 3\sigma$ detections or 3σ upper limits.
[c] Limits are given at 0.1 and 0.2 arcsec separations.

target and 7.5 minutes on each calibrator. The raw visibility data were calibrated with the MIR reduction package.[11] The passband was flattened using ∼1 hr scans of 3c454.3 or 3c279. The absolute flux scale was determined through observations of either Uranus or Titan and is estimated to be accurate to 15%. The flux densities of detected sources were measured by fitting a point-source model to the visibility data using the uvmodelfit task in the Common Astronomy Software Applications package CASA,[12] while upper limits were derived from the rms of the visibility amplitudes. The rms noise of our SMA observations ranges from ∼0.4 to 2.0 mJy per beam.

We detected, at the 3σ level or better, four of the SMA targets: 5, 29, and 31 (from our own data) and object 9 from the archival data. Objects 2 and 26 from the literature take the number of (sub)millimeter detections to 6. The (sub)millimeter wavelength fluxes (and 3σ upper limits) for our sample are listed in Table 2. In Section 4.3, we use the (sub)millimeter wavelength photometry to constrain the masses of our transition disks.

3.3.2. JCMT Observations with SCUBA-2

The SCUBA-2 data were obtained in service mode on 2010 February 28 and March 1 during shared-risk observations using only one of the four arrays per channel of the final SCUBA-2 instrument (Holland et al. 2006). Each of the five objects observed with SCUBA-2 (targets 6, 8, 37, 38, and 40) was scanned following a daisy pattern for 15–25 minutes. During both nights the weather was quite good ($\tau_{225} = 0.06$–0.08); however, both the 450 and 850 μm arrays were significantly

---

[11] Available at http://cfa-www.harvard.edu/∼cqi/mircook.html

[12] Available a http://casa.nrao.edu/casa_obtaining.shtml

noisier than expected during shared-risk observations. The strong quasars 3C 84 and 3C 111 were used as calibrators. The data were reduced using the Submm User Reduction Facility (SMURF[13]). None of the SCUBA-2 targets were detected in the final mosaics, where the rms noise at 850 μm is in the $\sim$5–10 mJ range. The 450 μm mosaics are much noisier (rms $\gtrsim$ 100 mJy) and have little value for our program. The 3σ upper limits at 850 μm for our SCUBA-2 targets are listed in Table 2.

4. RESULTS

4.1. Spectral Types and PMS Identification

We estimate the spectral types of our targets by comparing temperature-sensitive features in our echelle spectra to those in templates from stellar libraries. We use the libraries presented by Soubiran et al. (1998) and Montes (1998). The former has a spectral resolution of 42,000 and covers the entire 4500–6800 Å spectral range. The latter has a resolution of 12,000 and covers the 4000–9000 Å spectral range with some gaps in the coverage. Before performing the comparison, we normalize all the spectra and take the template and target to a common resolution. M-type stars were assigned spectral types based on the strength of the TiO bands centered around 6300, 6700, 7150, and 7800 Å. We classify G–K stars based on the ratio of the V I (at 6199 Å) to Fe I (6200 Å) line (Padgett 1996) and/or on the strength of the Ca I (6112 A) and Na I (5890 and 5896 Å) absorption lines (Montes et al. 1999; Wilking et al. 2005). The F, A, and B stars were identified and typed by the width of the underlying Hα absorption line (which is much wider than its emission line) and/or by the strength of the Paschen 16, 15, 14, and 13 lines. The spectral types so derived are listed in Table 2. We estimate the typical uncertainties in our spectral classification to be one spectral subclass for M-type stars and two spectral subclasses for K and earlier type stars. Spectral types for most of our targets in Perseus (the IC 348 members) and Taurus are presented in Luhman et al. (2003), Rebull et al. (2010), and/or Luhman et al. (2010). We find that most of our spectral types do in fact agree within one or two spectral subclasses with previously published values.

Background objects are known to contaminate samples of *Spitzer*-selected YSOc (Harvey et al. 2007; Oliveira et al. 2009; Papers I and II). At low flux levels, background galaxies are the main source of contamination. However, the optical and near-IR flux cuts we have implemented as part of our sample selection criteria are very efficient at removing extragalactic sources from the *Spitzer* catalogs. At the bright end of the flux distribution, AGB stars are the main source of contamination. AGB stars are surrounded by shells of dust and thus have small, but detectable, IR excesses. The extreme luminosities ($\sim 10^4$ $L_\odot$) of AGB stars imply that they can pass our optical and near-IR flux cuts even if they are located several kpc away. AGB stars can easily be identified in our sample as late M-type stars lacking both Hα emission (from either accretion or chromospheric activity) and Li I λ6707 absorption. We find six such objects in our sample, all in the Taurus region. Their full optical spectra are shown in Figure 2. As seen in Figure 1, the contamination of AGB stars is particularly high in the [3.6]–[24] color range between 1.5 and 2.5 (five of the six AGB stars fall in this narrow range).

The Li I λ6707 absorption line is a very good indicator of stellar youth in mid-K to M-type stars because Li is burned very efficiently in the convective interiors of low-mass stars and is depleted soon after these objects arrive on the MS (Cargile et al. 2010); however, it is not an age discriminant for early-type stars where the depletion timescales can approach the MS ages. To establish whether our early-type targets are in fact consistent with pre-main-sequence (PMS) stars associated with the Perseus, Taurus, and Auriga molecular clouds, we place them in the Hertzsprung–Russell (H-R) diagram (see Figure 3) and compare their position against the theoretical isochrones from Siess et al. (2000). We adopted the bolometric corrections and temperature scale from Kenyon & Hartmann (1995) and the following distances: 320 pc for Perseus (Herbig 1998), 140 pc for Taurus (Kenyon et al. 2008), and 300 pc for Auriga (Heiderman et al. 2010). We corrected for extinction using $A_J = 1.53 \times E(J - K_S)$, where $E(J - K_S)$ is the observed color excess with respect to the expected photospheric color for the given spectral type (also from Kenyon & Hartmann 1995). We find that five of our early-type (F5 to B9) targets fall below the 10 Myr isochrone (11, 30, 35, 36, and 38). All of them have very low disk luminosities and could be background MS stars with debris disks. MS stars in this temperature range are 2.5–100 times more luminous than the Sun and can be seen at large distances. Their large luminosities also imply that their debris disks are more likely to be detectable at *Spitzer* wavelengths because the fractional disk luminosity needed to produce a detectable 24 μm excess is much lower for BAF-type stars than it is for lower luminosity objects (Cieza et al. 2008a). However, object 11 in Perseus has been identified as a member of the IC 348 cluster (Luhman et al. 2003) based on proper-motion measurements. Given the uncertainties associated with placing objects in the H-R diagram, we consider object 11 to be a PMS star. In Section 5.1, we classify the other four underluminous objects as MS debris disk candidates.

The H-R diagram also serves as an independent check for our sample of late-type targets. As seen in Figure 3, all the K- and M-type objects fall within the 0.5 and 10 Myr isochrones, except for five of the six AGB stars that are clearly too overluminous to be low-mass objects at the distance of the Taurus molecular cloud. Setting aside six AGB stars (targets 25, 27, 34, 37, 39, and 40) and four likely MS stars (sources 30, 35, 36, and 38), we are left with 31 objects that constitute our sample of transition disks around bona fide PMS stars.

Unlike Papers I and II, where we found that virtually all the objects were K- and M-type stars, here we find that $\sim$30% of the bona fide transition objects (9/31) are BAFG-type stars. This difference is likely to be due to a combination of several effects. First, the initial mass function (IMF) is not the same in all the clouds. Lupus and Ophiuchus contain a larger proportion of very low mass stars (i.e., late M-type objects) than Taurus (Hughes et al. 1994; Erickson et al. 2011). Second, many low-mass objects at the distance of Perseus and Auriga (300–320 pc) are too faint to meet all of our sample selection criteria. Finally, there are significant differences in the sizes of the PMS populations. Since there are $\sim$3 more YSOc in Perseus than in Lupus, Perseus should contain a larger number of high-mass stars for a given IMF.

4.2. Hα Profiles and Accretion Rates

Most young low-mass stars show Hα emission, from either chromospheric activity or accretion. Non-accreting objects show narrow ($\lesssim$200 km s^{-1}, measured at 10% of the peak intensity) and symmetric line profiles of chromospheric origin, while accreting objects present broad ($\gtrsim$270 km s^{-1}) and asymmetric

---

[13] http://www.starlink.ac.uk/docs/sun258.htx/sun258.html

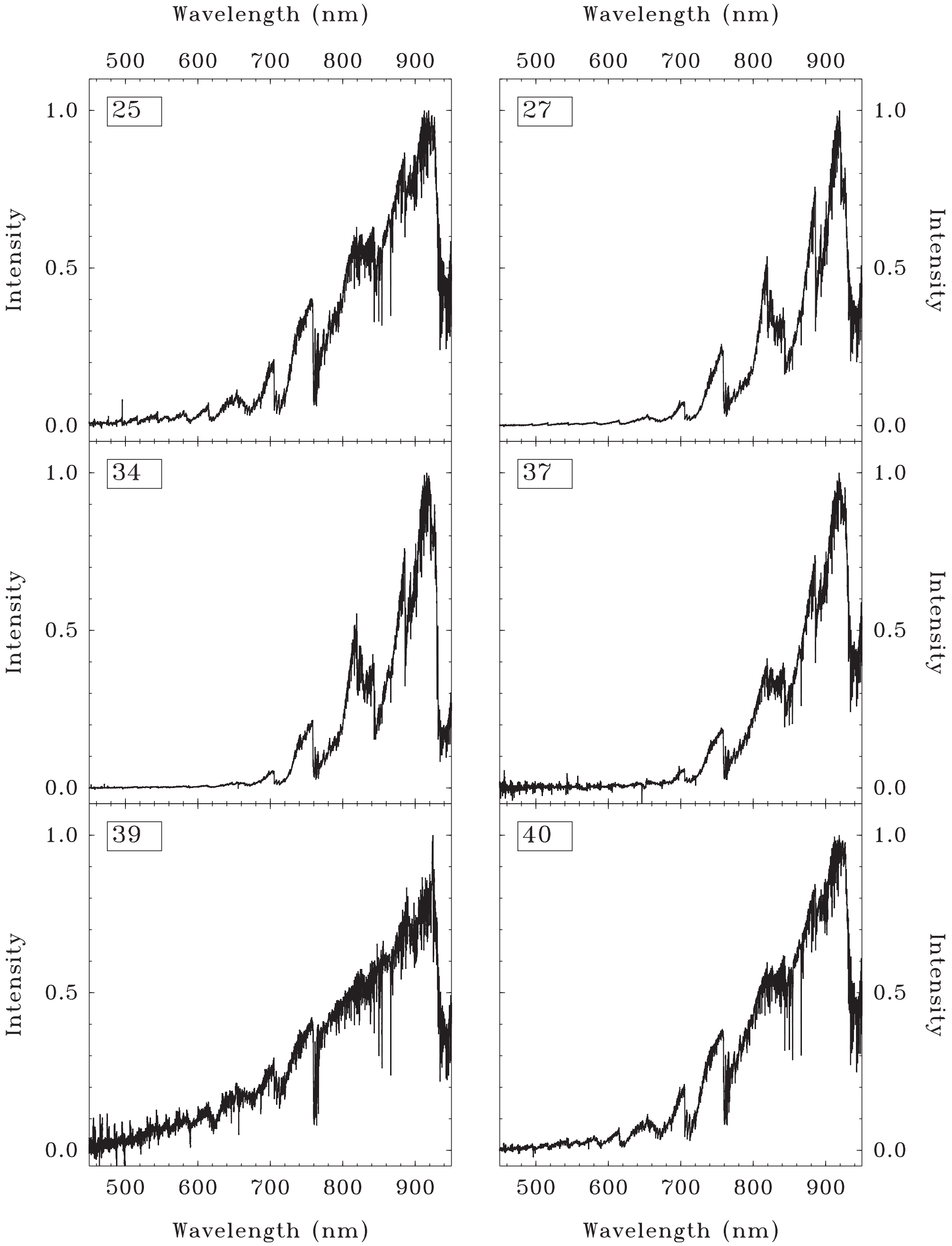

Figure 2. Optical spectra of the six AGB stars contaminating our sample.

profiles produced by large-velocity magnetospheric accretion columns. In order to measure the velocity width of the Hα emission line, we first subtract the continuum by fitting a line to the spectrum in the velocity intervals -600 to -400 km s^{-1} and 400–600 km s^{-1} centered at the Hα location. The peak of the continuum-subtracted spectrum is then normalized to 1, and the velocity width, ΔV, is measured at 10% of the peak intensity. The velocity dispersion so derived for the Hα emission lines of our transition disks is listed in Table 2. We estimate the typical uncertainty in ΔV to be of the order of 10%. However, as discussed below, the uncertainty in the corresponding accretion rate is expected to be much larger.

The boundary between accreting and non-accreting objects has been empirically placed by different studies at ΔV between 200 km s^{-1} (Jayawardhana et al. 2003) and 270 km s^{-1} (White & Basri 2003). Since only two objects, sources 20 and 23, have ΔV in the 200–270 km s^{-1} range, most accreting and non-accreting objects are clearly separated in our sample. Source 20 is an M6 star with a rising mid-IR SED, a 70 μm detection, and $\Delta V \sim$ 210 km s^{-1}. Very low mass stars tend to have narrower Hα lines than higher mass objects because of their lower accretion rates (Natta et al. 2004) and their lower gravitational potentials (Muzerolle et al. 2003). Given all the available data, we classify target 20 as an accreting object but warn the reader that its accreting nature is less certain than that of the rest of the objects classified as CTTSs. Similarly, source 23 has $\Delta V \sim 200$ km s^{-1} and we consider it to be non-accreting because of its very low fractional disk luminosity ($L_D/L_* < 10^{-3}$; see Section 4.5), and it is likely to be an optically thin debris disk; however, its non-accreting nature is not certain. The continuum-subtracted

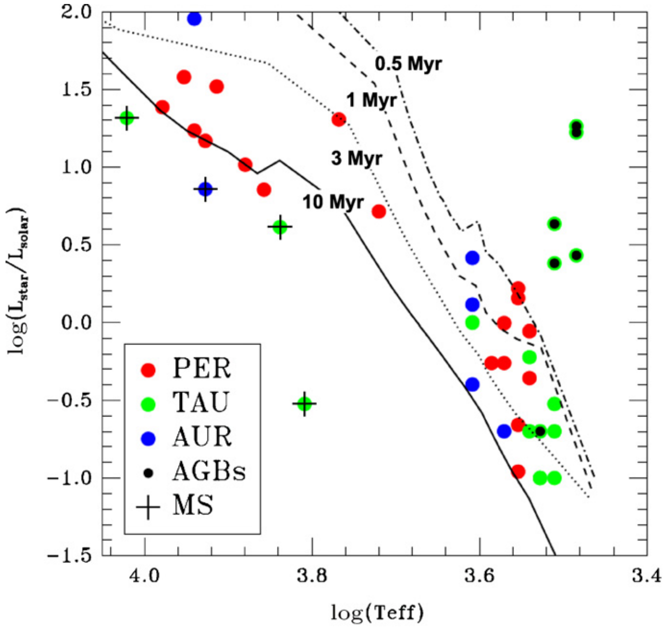

Figure 3. Location of all our targets in the H-R diagram. The 0.5, 1, 3, and 10 Myr isochrones from the Siess et al. (2000) models are also shown. Five of the six AGB stars are clearly overluminous (targets 25, 27, 34, 37, and 40). Three stars in Taurus (35, 36, and 38) and one in Auriga (30) are significantly underluminous and are likely to be background MS stars. One target in Perseus (11) is also slightly underluminous, but it has been classified as a member of the IC 348 cluster based on proper-motion measurements (Luhman et al. 2003).

(A color version of this figure is available in the online journal.)

Hα profiles for all 13 accreting transition disks are shown in Figure 4.

There are nine K- and M-type stars in our sample with narrow Hα emission consistent with chromospheric activity. The continuum-subtracted Hα profiles of these objects are shown in Figure 5. The spectra of targets 13 and 16 have lower signal-to-noise ratios than the rest of the spectra in the figure, which makes it difficult to measure accurate ΔV values. Target 13 is an M2 star with a small Hα equivalent width (3.5 Å; Luhman et al. 2003), and object 16 has $L_D/L_* < 10^{-3}$ and is another likely debris disk. For disk classification purposes, we consider both objects to be non-accreting. The 13 BAFG stars in our sample show the characteristic photospheric Hα line in absorption, with little or no evidence for significant superimposed Hα emission (see Figure 6). As discussed in the previous section, four of them are likely to be background MS stars (objects 30, 35, 36, and 38). The other nine objects are consistent with non-accreting PMS stars and are bona fide targets.

For accreting objects, the velocity dispersion of the Hα line correlates well with accretion rates derived from models of the magnetospheric accretion process. We therefore estimate the accretion rates of our targets from the width of the Hα line measured at 10% of its peak intensity, adopting the relation given by Natta et al. (2004):

$$\log(M_{\rm acc}(M_\odot\,{\rm yr}^{-1})) = -12.89(\pm 0.3) + 9.7(\pm 0.7) \times 10^{-3}\Delta V({\rm km\,s^{-1}}). \qquad (1)$$

This relation is valid for 600 km $s^{-1} > \Delta V >$ 200 km s^{-1} (corresponding to $10^{-7}\,M_\odot$ yr^{-1} > $M_{\rm acc}$ $10^{-11}\,M_\odot$ yr^{-1}) and can be applied to objects with a range of stellar (and substellar) masses. As discussed by Muzerolle et al. (2003) and Sicilia-Aguilar et al. (2006), the broadening of the Hα line is 1–2 orders of magnitude more sensitive to *low* accretion rates than other accretion indicators, such as U-band excess and continuum veiling measurements, and is thus particularly useful to distinguish weakly accreting from non-accreting objects. However, the 10% width measurements are also dependent on the line profile, rendering the 10% Hα velocity width a relatively poor *quantitative* accretion indicator (Nguyen et al. 2009).

For the objects we consider to be non-accreting, we adopt a mass accretion upper limit of 10^{-11} $M_\odot$ yr^{-1}, corresponding to ΔV = 200 km s^{-1}, although the detectability of accretion is a function of both spectral type and data quality. The so derived accretion rates (and upper limits) for our sample of transition disks are listed in Table 3. Given the large uncertainties associated with Equation (1) and the intrinsic variability of accretion in PMS stars, these accretion rates should be considered to be order-of-magnitude estimates.

4.3. Disk Masses

Disk masses obtained from modeling the IR and (sub)millimeter SEDs of circumstellar disks are well described by a simple linear relation between (sub)millimeter flux and disk mass (Andrews & Williams 2005, 2007). Following Papers I and II, we adopt the linear relations presented by Cieza et al. (2008b):

$$M_{\rm DISK} = 1.7 \times 10^{-1}\left[\left(\frac{F_\nu(1.3\,{\rm mm})}{\rm mJy}\right) \times \left(\frac{d}{140\,{\rm pc}}\right)^2\right] M_{\rm JUP} \qquad (2)$$

$$M_{\rm DISK} = 8.0 \times 10^{-2}\left[\left(\frac{F_\nu(0.85\,{\rm mm})}{\rm mJy}\right) \times \left(\frac{d}{140\,{\rm pc}}\right)^2\right] M_{\rm JUP}. \qquad (3)$$

These relations come from the ratios of model-derived disk masses to observed (sub)millimeter fluxes presented by Andrews & Williams (2005) for 33 Taurus stars. Based on the standard deviation in the ratios of the model-derived masses to observed (sub)millimeter fluxes, the above relation gives disk masses that are within a factor of ∼2 of model-derived values; nevertheless, much larger *systematic* errors cannot be ruled out (Andrews & Williams 2007). In particular, the models from Andrews & Williams (2005, 2007) assume an opacity as a function of frequency of the form $K_\nu \propto \nu$ and a normalization of $K_0 = 0.1$ gr cm^{-2} at 1000 GHz. This opacity implicitly assumes a gas-to-dust mass ratio of 100. Both the opacity function and the gas-to-dust mass ratio are highly uncertain and expected to change due to disk evolution processes such as grain growth and photoevaporation. Detailed modeling and additional observational constraints on the grain size distributions (e.g., from sub/millimeter wavelength slopes) and the gas content (e.g., from CO, [O I], and/or [C II] observations) will be needed to derive more accurate disk masses for each individual transition disk.

The disk masses (and 3σ upper limits) for our sample are listed in Table 3 and were derived adopting the distances to the clouds from Section 4.1. The vast majority of our transition objects have estimated disk masses lower than ∼1–3 $M_{\rm JUP}$. However, five of them have disk masses typical of CTTSs (∼3–15 $M_{\rm JUP}$).

4.4. Stellar Companions

From the visual inspection of our Gemini-AO images, we identify 13 multiple systems: targets 1, 4, 5, 14, 15, 18, 22,

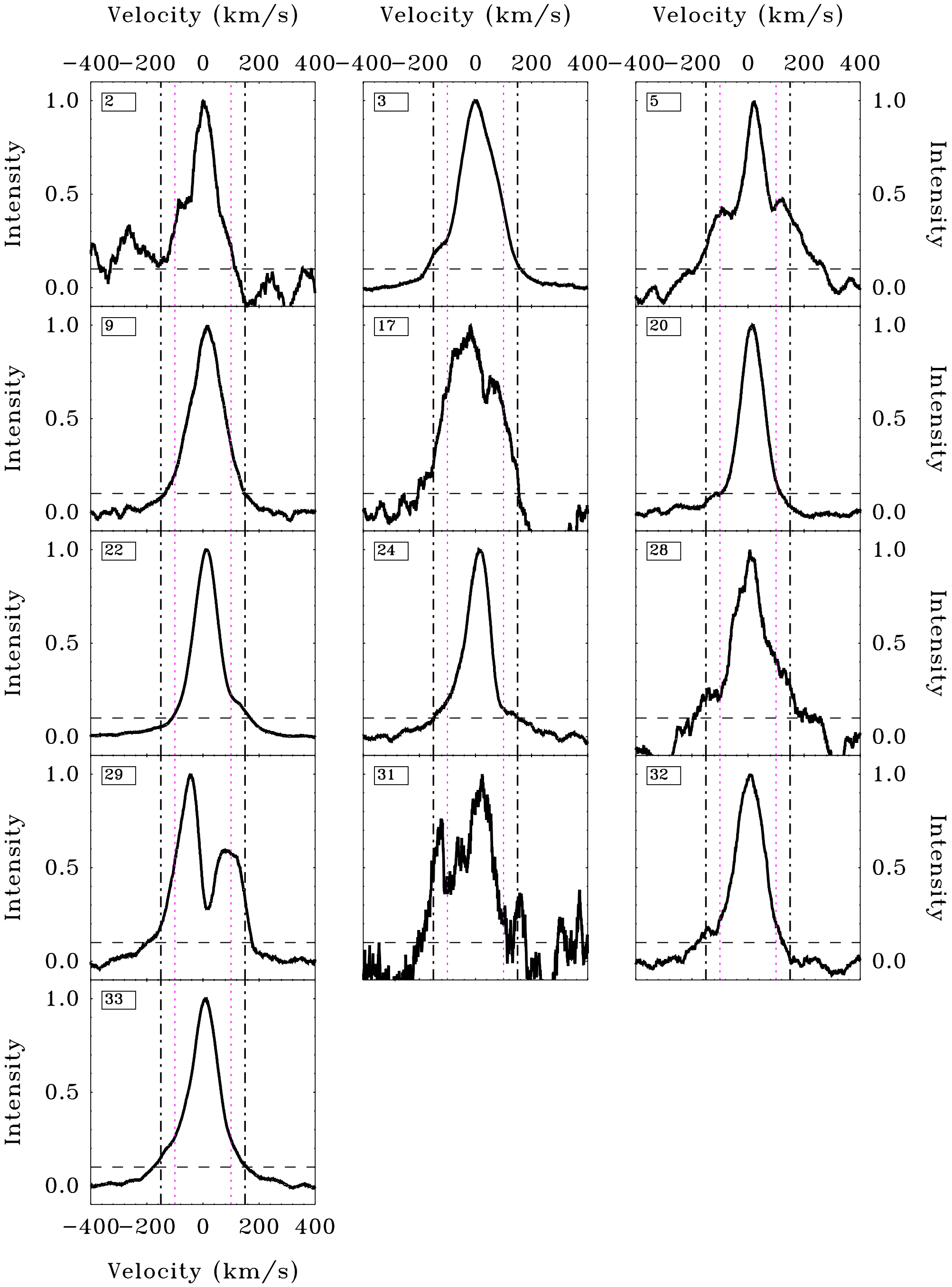

Figure 4. Hα velocity profiles of the 13 accreting objects in our sample. The dashed line indicates the 10% peak intensity, where ΔV is measured. The intervals delimited by the dotted and dash-dotted lines correspond to $\Delta V = 200$ and $\Delta V = 300$ km s^{-1}, respectively. All accreting objects have $\Delta V > 200$ km s^{-1}.

(A color version of this figure is available in the online journal.)

24, 26, 28, 31, 32, and 33 (see Figure 7). The separation and flux ratios of these systems range from 0.″05 to 1.″7 and 1.0 to 14, respectively. Object 1 is a triple. Most systems were fully resolved in both our J- and K_S-band images, which have typical FWHM values of 0.″06–0.″08. The tightest systems, targets 26 and 33, were only fully resolved by the J-band images (FWHM ∼ 0.″05).

In Perseus, targets 14 and 15 are previously known binaries (Duchêne et al. 1999), while targets 1, 4, 5, and 18 are newly identified multiple systems. Similarly, objects 24, 26, and 33 are known Taurus binaries (Konopacky et al. 2007; Simon et al. 1995), while target 22 is a newly discovered Taurus binary system. All three multiples in Auriga (objects 28, 31, and 32) are newly identified systems. For target 32, the AO system did not lock correctly in either of the two components of the binary, resulting in a very poor AO correction and a highly uncertain determination of the flux ratio.

For the apparently single stars, we estimated the detection limits at 0.″1 and 0.″2 separations from the 5σ noise of PSF-subtracted images. Since no PSF standards were observed in our program, we subtract a PSF constructed by azimuthally smoothing the image of the target itself, as follows. For each pixel in the image, the separation from the target's centroid is calculated, with sub-pixel accuracy. The median intensity

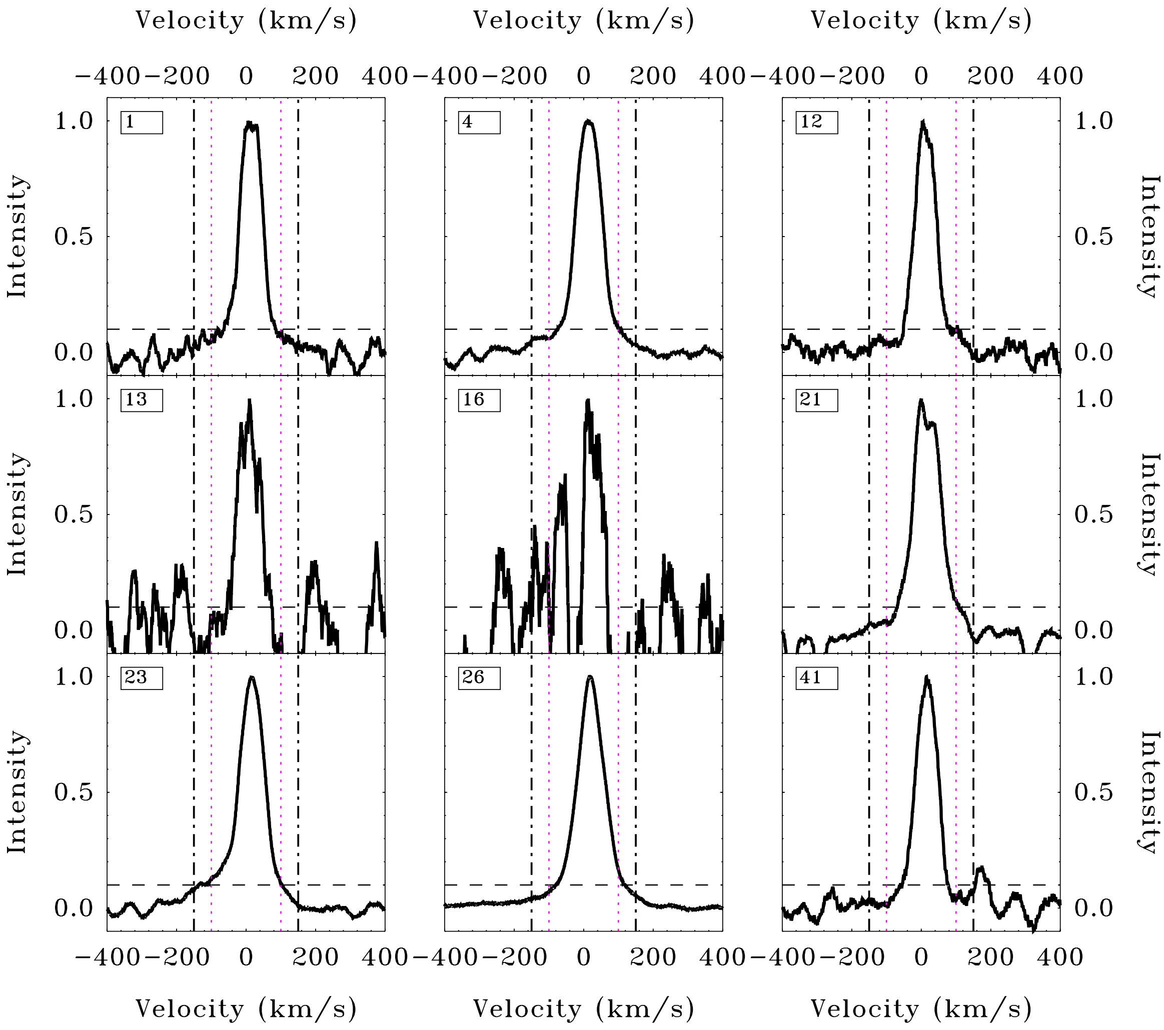

Figure 5. Hα velocity profiles of the nine non-accreting objects in our sample where Hα was detected in emission. They are all K- and M-type stars. The dashed line indicates the 10% peak intensity, where ΔV is measured. The intervals delimited by the dotted and dash-dotted lines correspond to $\Delta V = 200$ and $\Delta V = 300$ km s^{-1}, respectively. Non-accreting objects show symmetric and narrow ($\Delta V \lesssim 200$ km s^{-1}) Hα emission, consistent with chromospheric activity.

(A color version of this figure is available in the online journal.)

at that separation, but within an arc of 30 pixels in length, is then subtracted from the target pixel. Thus, any large-scale, radially symmetric structures are removed. The separations, positions angles, and flux ratios of the multiple systems in our sample are shown in Table 2. The flux ratio limits for unseen companions at 0$''$.1 and 0$''$.2 separations, obtained as described above, are also listed for the targets that appear to be single.

4.5. SED Morphologies and Fractional Disk Luminosities

In addition to the disk mass, accretion rate, and multiplicity, the SED morphology and fractional disk luminosity of a transition disk can provide important clues on the nature of the object. Following Papers I and II, we quantify the SED morphologies and fractional disk luminosities of our transition objects and use these quantities as part of our disk classification scheme (see Section 5.1). We quantify the SED "shape" of our targets adopting the two parameters introduced by Cieza et al. (2007): $\lambda_{\text{turn-off}}$, which is the longest wavelength at which the observed flux is dominated by the stellar photosphere, and α_{excess}, the slope of the IR excess, computed as $d\log(\lambda F)/d\log(\lambda)$ between $\lambda_{\text{turn-off}}$ and 24 μm. To calculate $\lambda_{\text{turn-off}}$, we compare the extinction-corrected SED to NextGen Models (Hauschildt et al. 1999) normalized to the J band and choose $\lambda_{\text{turn-off}}$ as the longest wavelength at which the stellar photosphere contributes over 50% of the total flux. The uncertainty of $\lambda_{\text{turn-off}}$ is roughly one SED point. The $\lambda_{\text{turn-off}}$ and α_{excess} values for our entire sample are listed in Table 3. The $\lambda_{\text{turn-off}}$ and α_{excess} parameters are dependent on the SED sampling and are affected by IR variability (Espaillat et al. 2011); however, they provide first-order information on the structure of the disk. For a given stellar luminosity, the $\lambda_{\text{turn-off}}$ value correlates with the size of the inner hole as it depends on the temperature of the dust closest to the star. It is clear, however, that a given $\lambda_{\text{turn-off}}$ value implies a much larger inner hole for a disk around an A-type star than for one around an M-type star. Similarly, α_{excess} correlates well with the sharpness of the opacity hole. On the one hand, sharp inner holes result in positive α_{excess} values, which are typical of classical transition disks (Muzerolle et al. 2010) and cold disks (Brown et al. 2007; Merín et al. 2010) with rising mid-IR SEDs. On the other hand, more radially continuous disks that have undergone significant grain growth and dust settling show the negative α_{excess} values (Dullemond & Dominik 2004) that are characteristic of anemic (Lada et al. 2006) and homologously depleted (Currie et al. 2009) transition disks with falling mid-IR SEDs. See Espaillat

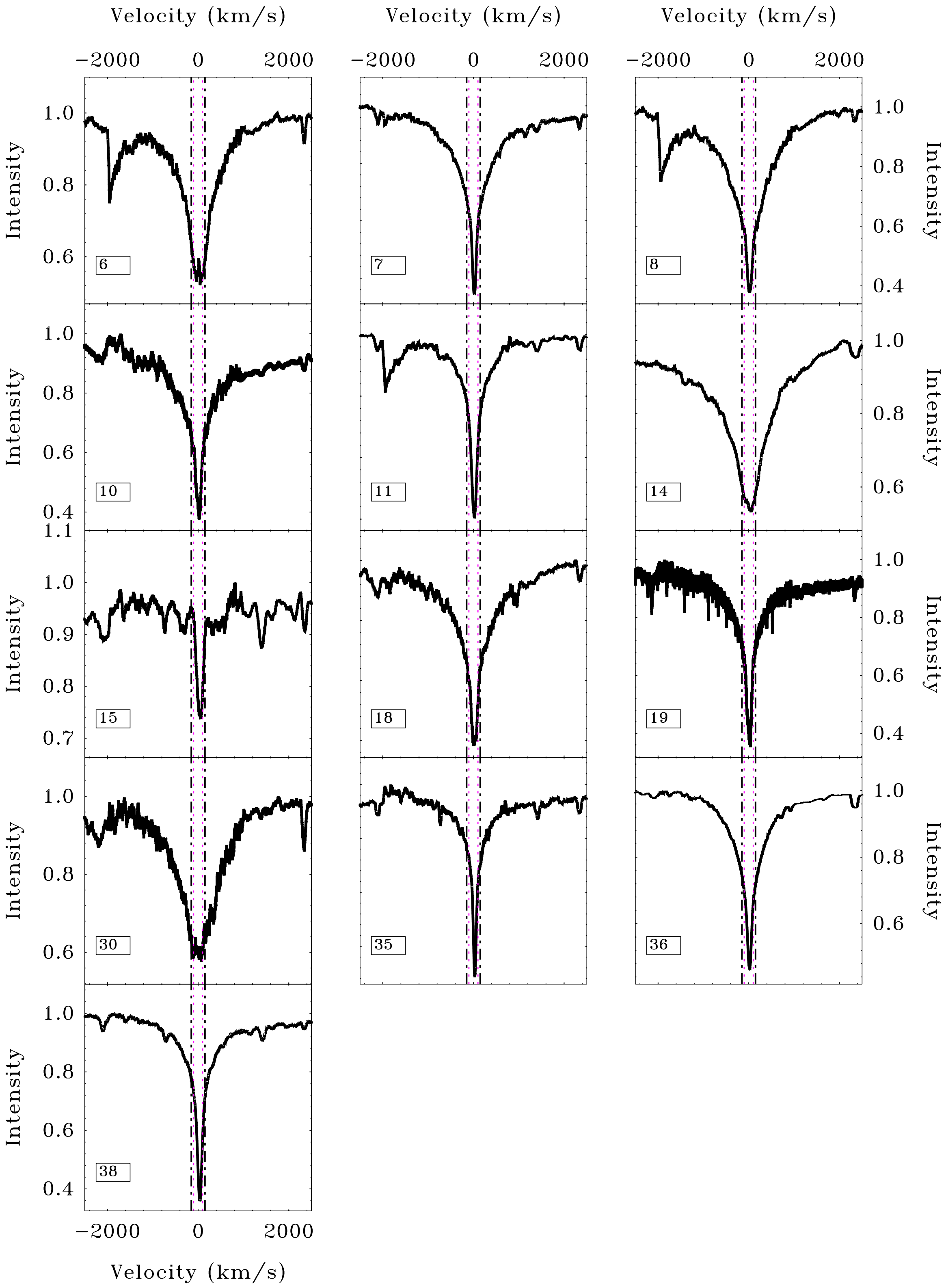

Figure 6. Hα profiles of the 13 non-accreting objects in our sample where Hα was detected in absorption. They are all BAFG-type stars.

(A color version of this figure is available in the online journal.)

et al. (2012) for a recent discussion on the link between SED morphology and physical properties of the disk.

The fractional disk luminosity, the ratio of the disk luminosity to the stellar luminosity (L_D/L_*), is another important quantity that relates to the evolutionary state of a disk. Typical primordial disks around CTTSs have $L_D/L_* \sim 0.1$ as they have optically thick disks that intercept (and reemit in the IR) ~10% of the stellar radiation. In contrast, debris disks show L_D/L_* values $\lesssim 10^{-3}$ because they have optically thin disks that intercept and reprocess $\sim 10^{-5}$–10^{-3} of the star's light (Bryden et al. 2006).

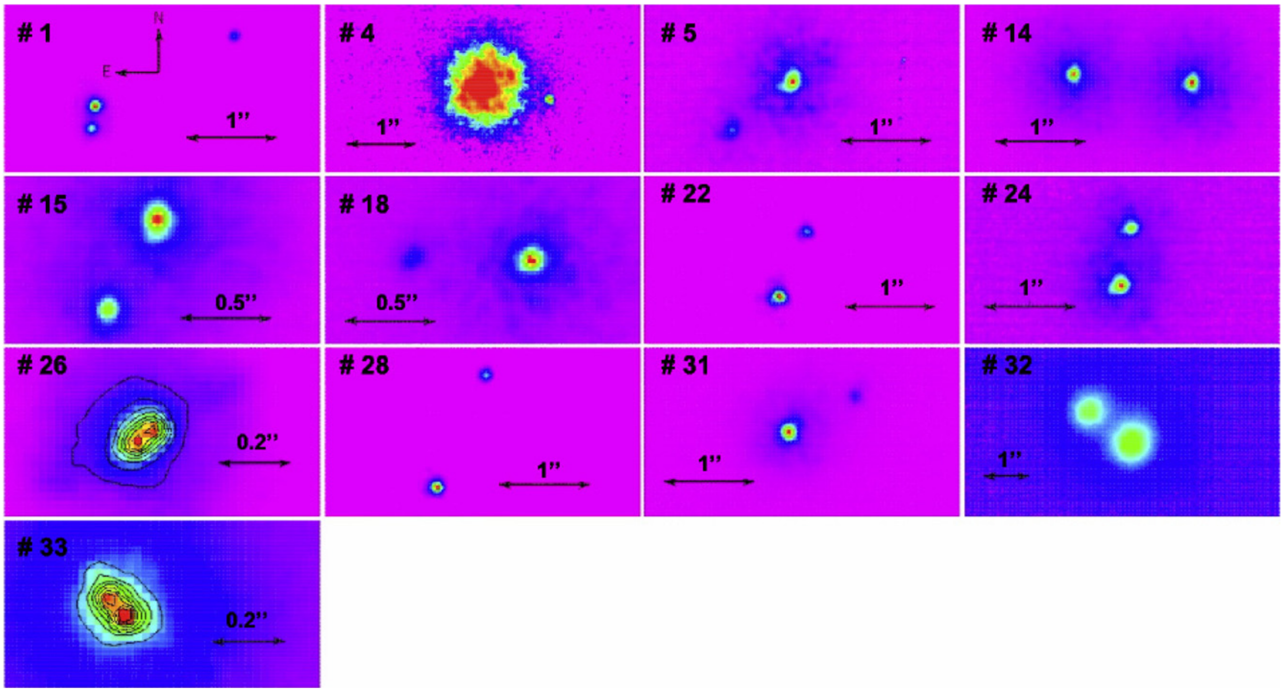

Figure 7. AO images of the 13 multiple systems that have been detected with our Gemini observations. Target 1 is a triple system. The images shown correspond to the K band, except for objects 26 and 33, for which the J-band images are shown because they have a somewhat higher spatial resolution.

(A color version of this figure is available in the online journal.)

We estimate L_D/L_* for our sample of disks by integrating over frequency the flux contribution of the disk and the star to the observed SED (see Paper I for calculation details). The near and mid-IR luminosities of our disks are well constrained because their SEDs are relatively well sampled at these wavelengths. However, their far-IR luminosities remain more poorly constrained. Only 5 of our 41 targets have (5σ or better) detections at 70 μm listed in the *C2D*, *Goulds Belt*, and *Taurus* catalogs. For the rest of the objects, we have obtained 5σ upper limits as in Paper I (from the noise of the 70 μm images at the location of the targets) in order to fill the gap in their SEDs between 24 μm and the millimeter.

The log(L_D/L_*) values for our transition disk sample, ranging from −1.7 to −4.9, are listed in Table 3. The log(L_D/L_*) values are highly dependent on SED sampling and should be considered order-of-magnitude estimates. As most of the luminosity of a disk extending inward to the dust sublimation temperature is emitted in the near-IR, L_D/L_* is a very strong function of $\lambda_{\text{turn-off}}$: the shorter the $\lambda_{\text{turn-off}}$ wavelength, the higher the fractional disk luminosity. For objects with $\lambda_{\text{turn-off}} < 8.0\,\mu$m, the 70 μm flux represents only a minor contribution to the total disk luminosity. On the other hand, objects with $\lambda_{\text{turn-off}} = 8.0\,\mu$m (i.e., objects where the IR excess only becomes significant at 24 μm) have much lower L_D/L_* values, and the 70 μm emission becomes a much larger fraction of the total disk luminosity. As a result, the L_D/L_* values of objects with $\lambda_{\text{turn-off}} = 8.0\,\mu$m and no 70 μm detections should be considered upper limits.

5. DISCUSSION

5.1. Disk Classification

One of the main results from Papers I and II has been the very large range of disk properties (accretion rates, disks masses, SED morphologies, and L_D/L_* values) exhibited by our targets. This diversity points toward different evolutionary stages and/or different physical processes driving the evolution of each disk.

In particular, the wealth of information discussed in the previous sections allows us to place each target in our transition sample into the following categories: grain-growth-dominated disks, giant planet-forming disks, photoevaporating disks, debris disks, and circumbinary disks.

5.1.1. Grain-growth-dominated Disks

Accreting objects with $\alpha_{\text{excess}} < 0$ (falling mid-IR SEDs) are most readily explained as primordial disks that have undergone significant grain growth and dust settling. The SEDs of the seven transition disks in this category are shown in Figure 8. Circumstellar disks are initially very flared and intersect a significant fraction of the stellar radiation, most of which is reprocessed and reemitted at IR wavelengths. As dust grains coagulate and grow in the disk, they fall toward the mid-plane, where the surface density is higher and they can grow at a higher rate and settle even deeper into the disk. As a result, the disk becomes geometrically flatter with time, which reduces the fraction of stellar radiation intercepted by the disk and steepens the slope of the SED at mid-IR wavelengths (D'Alessio et al. 2006; Dullemond et al. 2007). Grain growth is expected to proceed faster in the inner disk, where the surface densities are higher and the dynamical timescales are shorter. Thus, the depletion of micron-sized grains in the inner disk through grain growth also contributes to the low levels of near-IR and mid-IR excesses seen in this type of object (Dullemond & Dominik 2005).

Based on their SEDs, grain-growth-dominated disks could also be classified as anemic (Lada et al. 2006) or homologously depleted transition disks (Currie et al. 2009). They show a large diversity of accretion rates and disk masses, which in this paper range from $10^{-10.3}$ to $10^{-8.5}$ $M_\odot$ yr^{-1} and <0.5 to 5.3 M_{JUP} (but note DoAr 25 in Paper I, with a disk mass of ∼40 M_{JUP}

Table 3
Derived Properties

No.	Log(Acc. Rate)[a] ($M_\odot$ yr^{-1})	Mass Disk[b] ($M_{\rm JUP}$)	$r_{\rm proj.}$ (AU)	$\lambda_{\rm tun-off}$[c] (μm)	$\alpha_{\rm excess}$	log(L_D/L_*)[d]	A_J (mag)	Object Type
1	<−11.0	<2.6	62; 425	5.8	−1.19	−2.89	0.6	Photoevaporating disk
2	−10.2	5.6	...	5.8	0.69	−2.33	1.3	Giant planet-forming disk
3	−9.6	<2.7	...	3.6	−0.95	−1.72	0.1	Grain-growth-dominated disk
4	<−11.0	<2.6	240	8.0	−1.69	<−3.57	0.5	Debris disk
5	−8.5	5.3	212	5.8	−0.80	−2.56	0.5	Grain-growth-dominated disk
6	<−11.0	<6.2	...	5.8	−1.68	−4.27	0.8	Debris disk
7	<−11.0	<2.7	...	5.8	0.11	−2.09	0.1	Photoevaporating disk
8	<−11.0	<6.2	...	5.8	−1.74	−4.09	0.8	Debris disk
9	−10.2	13.0	...	5.8	0.49	−2.19	0.7	Giant planet-forming disk
10	−10.9	...	...	5.8	−2.12	−4.39	0.4	Debris disk
11	<−11.0	...	...	8.0	−1.87	<−3.40	0.1	Debris disk
12	<−11.0	<2.70	...	8.0	−0.20	<−2.41	0.5	Photoevaporating disk
13	<−11.0	<1.3	...	5.8	0.33	−2.92	1.5	Photoevaporating disk
14	<−11.0	<2.5	327	3.6	−0.76	−2.37	0.5	Photoevaporating disk
15	<−11.0	<2.6	140	4.5	−1.75	−2.80	1.0	Photoevaporating disk
16	<−11.0	<2.2	...	8.0	−0.95	<−3.03	2.0	Debris disk
17	−9.4	<1.0	...	4.5	−0.35	−2.26	1.2	Giant planet-forming disk
18	<−11.0	...	162	8.0	−2.03	<−4.05	0.5	Debris disk
19	<−11.0	<3.0	...	8.0	−1.63	<−4.88	0.4	Debris disk
20	−10.85	<0.6	...	8.0	0.83	−2.14	0.6	Giant planet-forming disk
21	<−11.0	<0.9	...	8.0	−1.55	<−3.90	0.5	Debris disk
22	−10.3	<0.50	108	5.8	−1.42	−2.57	0.0	Grain-growth-dominated disk
23	<−11.0	...	...	8.0	−1.91	<−3.78	0.4	Debris disk
24	−10.0	<0.50	90	4.5	−1.18	−2.33	1.2	Grain-growth-dominated disk
25	...	...	...	5.8	−0.95	...	...	AGB star
26	<−11.0	0.4	7	8.0	−1.88	<−2.77	0.0	Photoevaporating/circumbinary disk
27	<−11.0	<1.0	...	8.0	−1.97	...	...	AGB star
28	−9.3	<2.6	390	8.0	−0.90	<−2.53	1.1	Grain-growth-dominated disk
29	−9.3	7.5	...	5.8	0.38	−2.62	0.7	Giant planet-forming disk
30	<−11.0	<2.6	...	8.0	−1.39	<−4.28	0.7	MS debris disk
31	−9.5	3.7	249	5.8	0.90	−2.15	1.3	Giant planet-forming disk
32	−9.9	<1.9	360	5.8	−1.05	−2.73	0.6	Grain-growth-dominated disk
33	−9.7	<2.9	10	5.8	−0.99	−2.37	0.3	Grain-growth-dominated disk
34	...	<0.8	...	3.6	−0.99	...	...	AGB Star
35	<−11.0	...	...	8.0	−1.32	<−3.65	0.7	MS debris disk
36	<−11.0	<0.5	...	5.8	0.09	−3.44	0.5	MS debris disk
37	...	...	...	8.0	−1.94	...	...	AGB Star
38	<−11.0	...	...	8.0	−1.71	<−3.15	0.0	MS debris disk
39	...	<0.6	...	8.0	−1.86	...	...	AGB Star
40	...	...	...	8.0	−1.93	...	...	AGB star
41	<−11.0	<0.5	...	8.0	−1.35	<−3.90	0.9	Debris disk

Notes.

[a] The uncertainties in the accretion rate are dominated by the calibration of Equation (1). The values should be considered order-of-magnitude estimates. See Section 4.2.

[b] Disk masses were derived using Equations (2) and (3) and should be within a factor of ∼2 of modeled derived masses; however, larger systematic errors cannot be ruled out due to uncertainties in dust opacities and gas-to-dust mass ratios. See Section 4.3.

[c] The uncertainty in $\lambda_{\rm tun-off}$ is one SED point. See Section 4.5.

[d] log(L_D/L_*) is highly dependent on the SED sampling and should be consider an order-of-magnitude estimate. See Section 4.5.

and an accretion rate of $10^{-7.2}$ $M_\odot$ yr^{-1}). Establishing whether the decrement of IR excess is mostly due to a reduction of the dust opacity, a reduction of the surface density in the disk, or purely geometrical effects requires resolved observations and/or detailed modeling of individual objects. In some cases, the weakness of the IR excess might be attributed to the very low luminosity of the central star (see Section 5.2.4).

5.1.2. Giant Planet-forming Disks

Accreting transition disks with sharp inner holes (i.e., $\alpha_{\rm excess} \gtrsim 0$; rising mid-IR SEDs) are currently considered the most likely sites for ongoing planet formation (Najita et al. 2007; Merín et al. 2010; Williams & Cieza 2011). The recent identification of planet candidates within the inner holes of the T Cha (Huélamo et al. 2011) and LkCa 15 disks (Kraus & Ireland 2012) strongly supports this interpretation. We find that six objects fall in this category (see Figure 9). The presence of accretion unambiguously identifies them as gas-rich primordial disks. The connection between rising mid-IR SEDs and the presence of a sharp inner hole (a large change in surface density over a small radial distance) is well established through both SED modeling (Brown et al. 2007; Calvet et al. 2002, 2005) and direct submillimeter imaging (Brown et al. 2009; Hughes et al. 2007, 2009). While, in addition to planet formation, other processes such as grain growth, photoevaporation, and

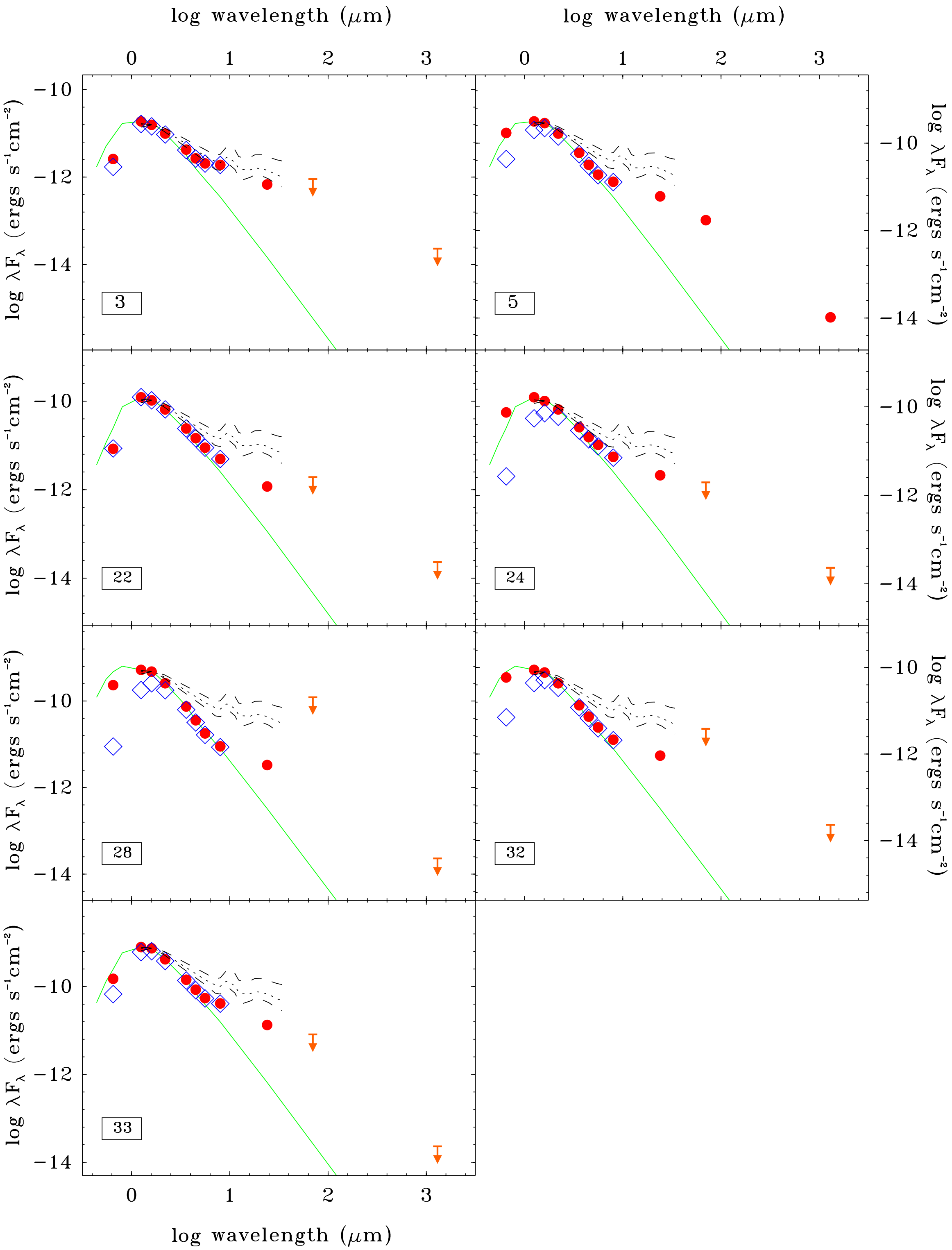

Figure 8. SEDs of the seven grain-growth-dominated disk candidates. The filled circles are detections, while the arrows represent 3σ limits. The open squares correspond to the observed optical and near-IR fluxes before being corrected for extinction using the A_J values listed in Table 3 (calculated as described in Section 4.1) and the extinction curve provided by the Asiago database of photometric systems (Fiorucci & Munari 2003). The solid green lines represent the stellar photosphere normalized to the extinction-corrected *J* band. The dotted lines correspond to the median mid-IR SED of K5–M2 CTTSs calculated by Furlan et al. (2006). The dashed lines are the quartiles.

(A color version of this figure is available in the online journal.)

dynamical clearing due to *stellar* companions have been proposed to explain this type of objects, these alternative explanations face serious theoretical and/or observational challenges. In particular, grain-growth efficiency is expected to be a smooth function of radius, which is inconsistent with the abrupt change in opacity inferred for transition disks with steeply rising mid-IR SEDs. Whether photoevaporation can account for the inner holes of accreting objects depends on the photoevaporation

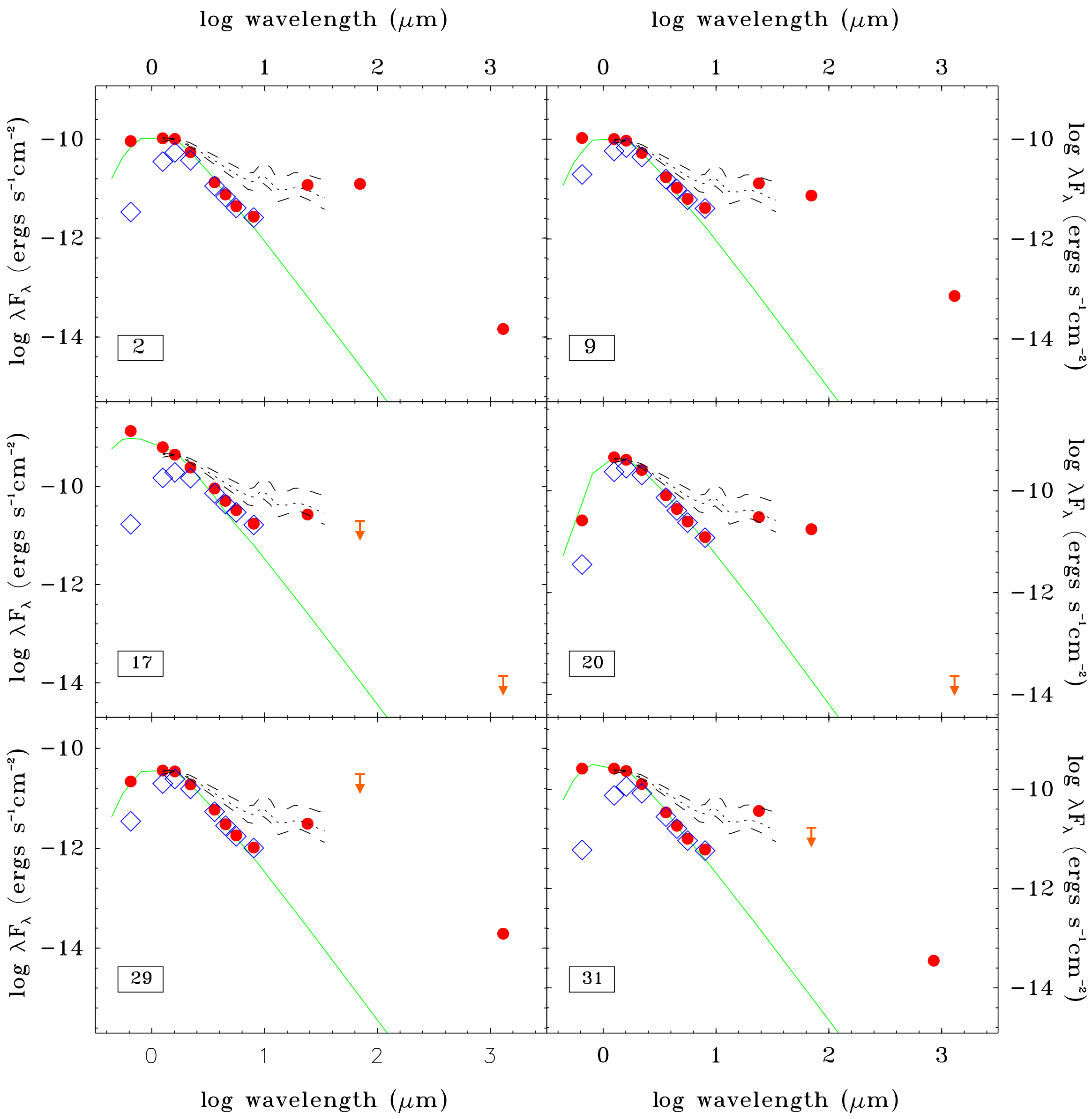

Figure 9. SEDs of the six giant planet-forming disk candidates. The symbols are the same as in Figure 8.

(A color version of this figure is available in the online journal.)

rates. As will be discussed in Section 5.2.3, there is strong evidence *against* photoevaporation rates being large enough to explain the inner holes of accreting transition disks. We thus conclude that the presence of accretion makes the photoevaporation scenario much less likely.

Dynamical clearing by (sub)stellar companions (Lubow & D'Angelo 2006; Zhu et al. 2011) therefore remains the most likely explanation for accreting transition disks with rising mid-IR SEDs. Recent hydrodynamical simulations of multiple planets embedded within the disk also help to reconcile the lack of near-IR excess with the levels of accretion seen in transition disks in this category. The optically thick but physically narrow tidal tails predicted by these simulations can transport significant amounts of material without overpredicting the IR excesses observed (Dodson-Robinson & Salyk 2011). While our AO observations cannot rule out the presence of stellar companions to our targets inward of ∼15–30 AU, near-IR interferometry (Pott et al. 2010) and aperture masking observations (Kraus et al. 2009) conclusively exclude *stellar* companions as a possible cause of the inner holes in several similar objects. All things considered, we conclude that the dynamical clearing by one or multiple planets is the most likely explanation for the properties of the six objects shown in Figure 9.

5.1.3. Photoevaporating and Debris Disks

We find that virtually all non-accreting objects remain undetected at millimeter wavelengths, implying dust masses below 6–10 $M_\oplus$ (corresponding to disk masses $\lesssim$2–3 $M_{\rm JUP}$ for a gas-rich disk with a gas-to-dust mass ratio of 100). Target 26 (FW Tau) with an estimated disk mass of 0.4 $M_{\rm JUP}$ is the only exception. All photoevaporation models predict the formation of a gap in the disk and the subsequent draining of the inner disk once most of the outer disk mass has been depleted and the accretion rate falls below the photoevaporation rate. Once this inner hole has formed, the high-energy photons can reach the inner edge of the disk unimpeded, and the disk quickly dissipates from the inside out. After the circumstellar gas photoevaporates, the small grains are removed by radiation pressure and Poynting–Robertson drag, leaving behind a gas-poor disk with large grains, planetesimals, and/or planets (i.e., a debris disk). In this context, the most fundamental difference between a photoevaporating disk and a young debris disk is the presence of primordial gas at large radii: if the inner hole is due to photoevaporation, the outer disk should remain gas-rich beyond the photoevaporation front. Since we lack information on the gas content in the outer disks of our targets, we adopt a less direct criterion based on the fractional disk luminosity, L_D/L_*, to tentatively distinguish primordial photoevaporating disks from debris disks.

As discussed in Section 4.5, typical primordial disks around CTTSs have $L_D/L_* \sim 0.1$ as they have optically thick disks that reprocess ∼10% of the stellar radiation, while debris disks show L_D/L_* values $\lesssim 10^{-3}$ because their optically thin disks only intercept $\sim 10^{-5}$–10^{-3} of the star's light (Bryden et al. 2006). Disks around young WTTSs have L_D/L_* values that fill the gap between those two regimes, suggesting they are an evolutionary link between the two stages (Padgett et al. 2006; Cieza et al. 2007; Wahhaj et al. 2010). Following Papers I and II, we classify as photoevaporating disk objects with $L_D/L_* \gtrsim 10^{-3}$ and as debris disk objects with $L_D/L_* \lesssim 10^{-3}$. The SEDs of our seven photoevaporating disk candidates are shown in Figure 10, while the SEDs of our 15 debris disk candidates are shown in Figure 11. The central objects of four of the debris disk candidates appear to be significantly underluminous in the H-R diagram (targets 30, 35, 36, and 38) and could be background MS stars (see Section 4.1). CO observations with the Atacama Large Millimeter/Submillimeter Array (ALMA) will be able to measure the gas content of all non-accreting disks and conclusively establish their primordial or debris disk status.

5.1.4. Circumbinary Disks

Early multiplicity surveys of PMS stars have shown that most stars in the solar neighborhood form in multiple systems (Leinert et al. 1993; Ghez et al. 1993; Simon et al. 1995). Since most of these binary systems have orbits with semimajor axes of the order of the typical sizes of circumstellar disks, the dynamical interaction of the stellar components with each other's disks has dramatic effects on disk devolution. The outer disks around the individual stars in a binary system are expected to be tidally truncated at a fraction (∼0.5) of the binary separation. Similarly, the circumbinary disk, if present, should have an inner radius ∼2× the semimajor axis of the system (Artymowicz & Lubow 1994). While it is not the only possible outcome, tidal truncation in binary systems is known to produce inner opacity holes resulting in transition disk SEDs. Such is the case of the famous CoKu Tau/4 system (Ireland & Kraus 2008).

In Section 4.4, we found that 13 of our targets are in fact multiple systems. We now discuss the likelihood of each system to retain a circumbinary disk responsible for the observed SEDs. Nine of the binary systems in our sample (objects 4, 5, 14, 15, 18, 22, 28, 31, and 32) have *projected* separations greater than 100 AU (see Table 3). These projected separations represent the minimum value of the current physical separation. Any circumbinary disk around such wide systems should have an inner hole $\gtrsim$200 AU and would most likely remain undetectable in our SEDs. Targets 1, 24, and 33 have companions at 62, 90, and 10 AU, respectively. However, they are all M-type stars with significant excesses at 8 μm, implying the presence of dust at separations of the order of a few AU or less. Also, their SEDs show no evidence for dynamically induced inner holes. We thus conclude that their transition disk status is not a result of their stellar companions. Object 26 (FW Tau), on the other hand, has a projected separation of only 7 AU and a weak 24 μm excess and is therefore fully consistent with a circumbinary disk. The FW Tau system shares some of the properties of Coku Tau/4, such as its very low disk mass ($\lesssim 0.5\ M_{\rm JUP}$) and the lack of detectable accretion. The lower luminosity of FW Tau (it is an M5 star) might explain its lower mid-IR excess with respect to CoKu Tau/4 even if their inner holes are of similar size. We classify FW Tau as both a circumbinary and a photoevaporating disk candidate as tidal truncation and photoevaporation are not mutually exclusive processes. An important caveat of the circumbinary disk classification is the lack of constraints for most of the sample on stellar companions with separations $\lesssim$10 AU, a range where ∼30% of all stellar companions are expected to be found (Duquennoy & Mayor 1991; Kraus et al. 2012). Future radial velocity and aperture masking observations are likely to increase the number of objects in the circumbinary disk category.

5.2. Implication for Disk Evolution

Combining our sample of 31 transition disks with those from Papers I and II results in a sample of 74 homogenously selected and characterized transition disk objects. In this section, we discuss the properties of the combined sample and the important clues transition disks can provide on different aspects of disk evolution.

5.2.1. The Incidence of Planet-forming Disk Candidates

We find that only ∼18% (13/74) of the transition disks in our combined sample have properties that are best explained by the dynamical interaction of recently formed giant planets. Calculating the overall incidence of planet-forming disk candidates among protoplanetary disks in nearby molecular clouds is non-trivial because the fraction of transition disks and AGB contamination vary greatly from cloud to cloud. We calculate this important quantity as follows: we exclude from our calculation the Taurus molecular cloud because its catalog does not provide a YSOc classification, which results in planet-forming disk fraction of 21.0% (12/57) among the remaining well-characterized transition disks. From Table 3 in Paper II, we find that these 57 objects have been drawn from a sample of 1059 YSOc in eight different molecular clouds (Lup I, III, IV, V, and VI, Ophiuchus, Perseus, and Auriga), of which 24.8% (263/1059) satisfy our main sample selection criteria ([3.6]–[4.5] < 0.25 and [3.6]–[24] > 1.5). We thus estimate the overall fraction of planet-forming disk candidates among YSOc to be $0.210 \times 0.248 = 5.2\%$. The YSOc catalogs are known to be contaminated by AGB stars, and this contamination is higher among objects with transition disk SEDs (AGB stars typically have photospheric near-IR colors and small 24 μm excesses). From the estimates in Paper II's Table 3, we find that the overall YSOc contamination by AGBs in the eight clouds we consider is 10.3%, while the contamination increases to 15.6% in the region of the color–color diagram occupied by transition disks. Correcting the statistics from AGB contamination decreases the incidence of transition disks in the YSOc sample to 23.3% (222/950). Similarly, the overall fraction of planet-forming disk candidates among YSOc decreases slightly to $0.210 \times 0.233 = 4.9\%$.

For comparison, the incidence of giant planets within 20 AU of mature solar-type stars is estimated to be ∼20% (Cumming et al. 2008). This discrepancy strongly suggests that not all giant planets embedded in a primordial disk result in clear observational signatures. The presence of "hidden planets" is

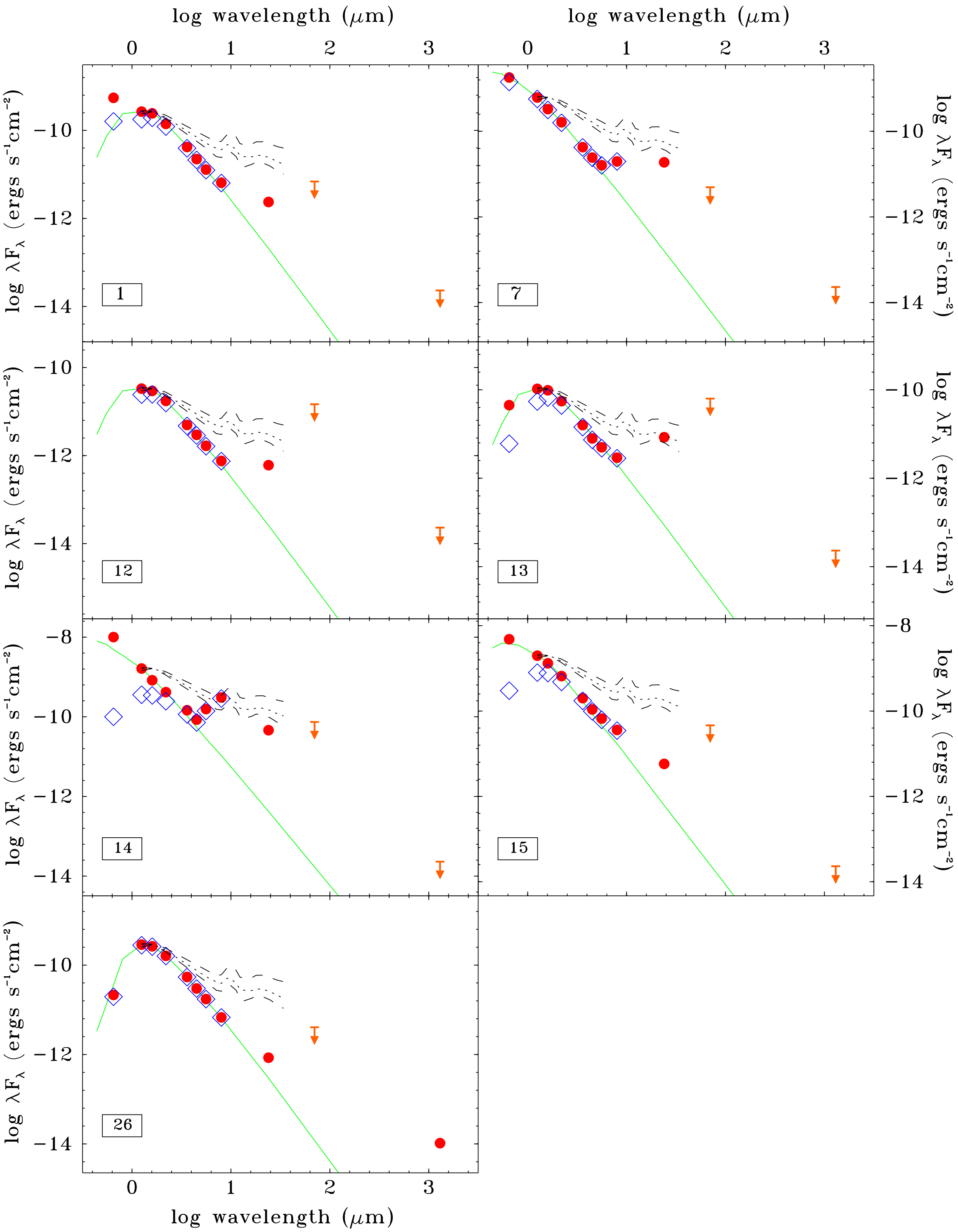

Figure 10. SEDs of the seven photoevaporating disk candidates. The symbols are the same as in Figure 8.

(A color version of this figure is available in the online journal.)

supported by the results from recent hydrodynamic simulations showing that multiple giant planets are needed in order to have a detectable effect in the emerging SED (Zhu et al. 2011; Dodson-Robinson & Salyk 2011). Furthermore, high-resolution (sub)millimeter images have revealed inner holes in systems that have perfectly "normal" SEDs (Andrews et al. 2011). This can easily be understood considering that (sub)millimeter observations can detect modest reductions in the surface density of the disk, while reducing the levels of the near-IR and mid-IR excess emission requires an extreme depletion of small dust particles. Also, the planet formation signature capture by our selection criteria is expected to be present for only a small fraction of the disk lifetime, after the planets have become massive enough to dynamically open a gap in the disk and the inner disk has drained. In other words, many protoplanetary disks with "normal" SEDs may contain one or more protoplanets

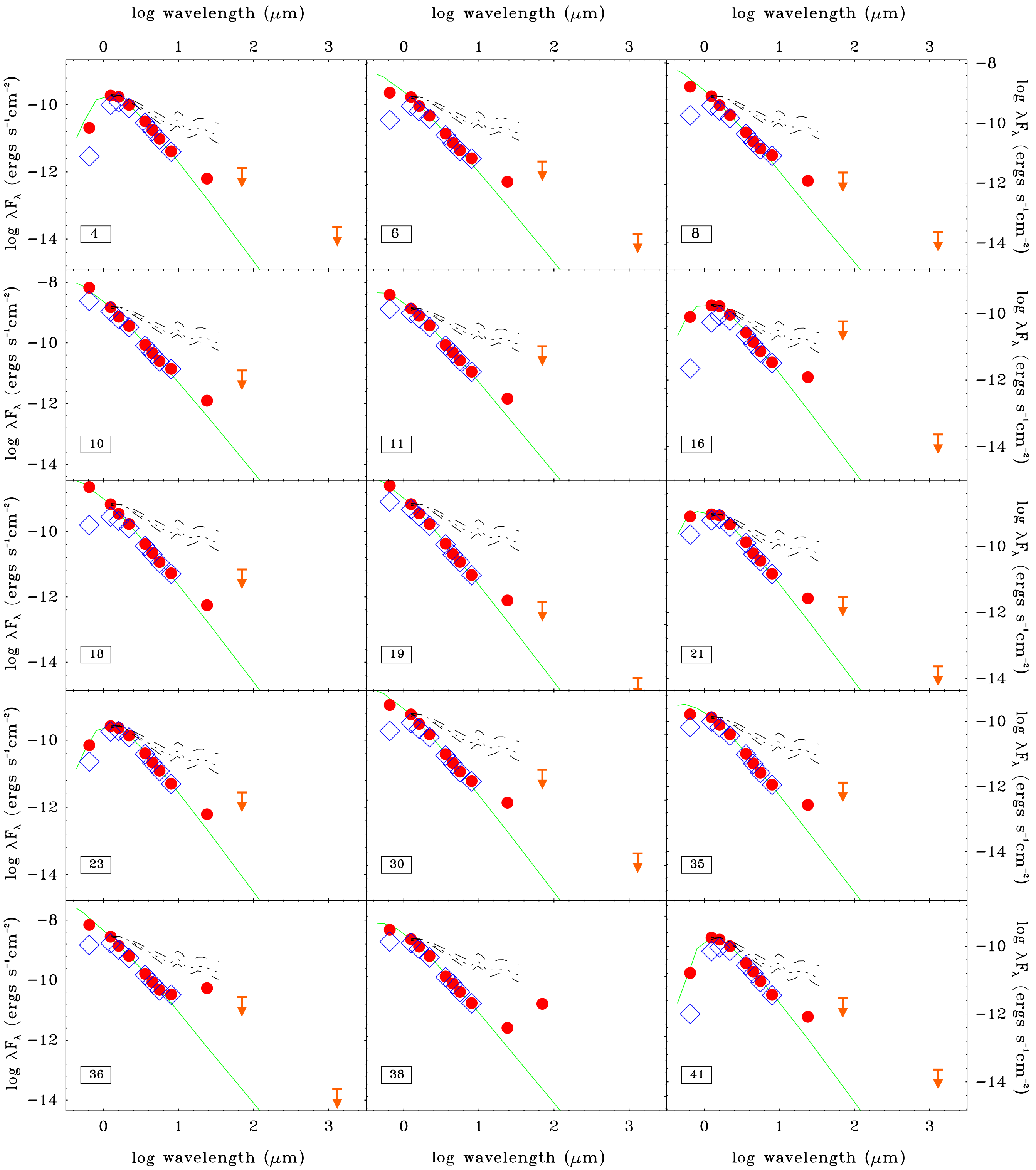

Figure 11. SEDs of the 15 debris disk candidates. All of them are non-accreting and have low disk masses ($\lesssim$5 $M_{\rm JUP}$) and/or fractional disk luminosities $L_{\rm disk}/L_{\rm star} < 10^{-3}$. As discussed in Section 4.1, objects 30, 35, 36, and 38 could be debris disks around early-type background MS stars.

(A color version of this figure is available in the online journal.)

that are not yet massive enough to open a wide hole in the disk, and as mentioned in Section 2, we are likely to miss pre-transition disks, with wide gaps but significant near-IR excess. We thus conclude that the giant planet disk candidates identified in our survey are likely to represent only a subsample of the entire population of disks actively forming planets in the molecular clouds we are considering. This subsample may be dominated by systems with multiple and/or very massive planets.

5.2.2. The Incidence of Circumbinary Disks

Dynamical clearing by stellar companions has been one of the main mechanisms proposed to explain the inner holes of transition disks. However, in Section 5.1 we only found one

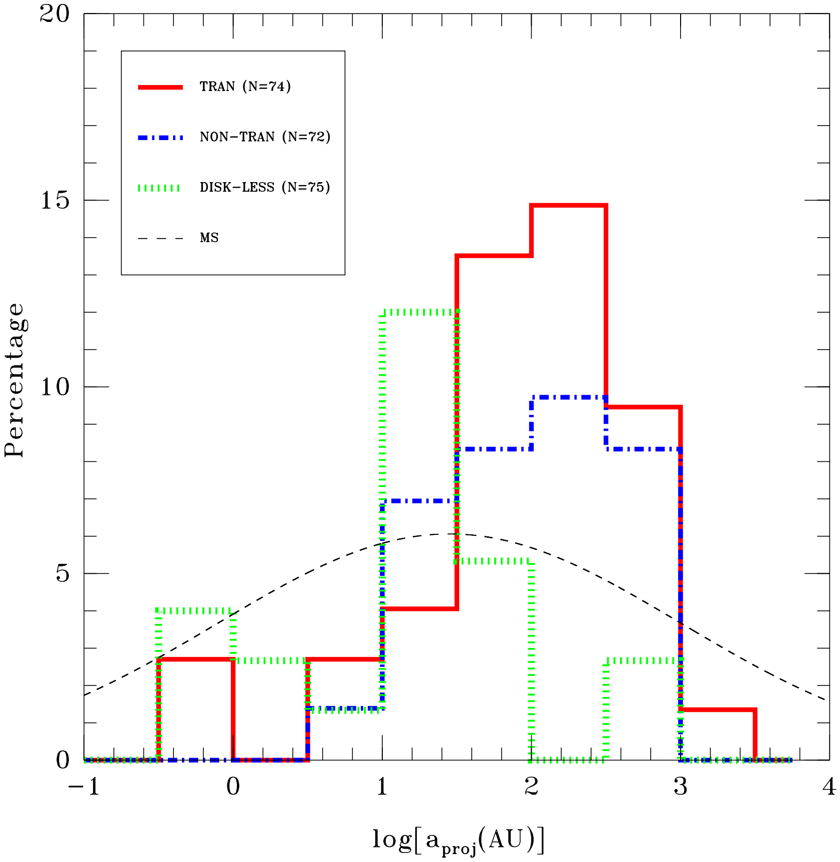

Figure 12. Distribution of *projected* companion separations for our combined transition disk sample (red solid line), non-transition disks from Cieza et al. (2009) (blue dash-dotted line), and diskless stars (green dotted line) also from Cieza et al. (2009). Spectroscopic binaries have been assigned a projected separation of 0.5 AU. The total number of objects (single + multiple systems) in each sample is shown in parentheses. The distribution of binary separations for main-sequence (MS) solar-type stars (Duquennoy & Mayor 1991) is shown for comparison. Binary systems with separations in the 10–30 AU range result in the rapid erosion of the individual circumstellar disks. Few circumbinary disks survive in such systems.

(A color version of this figure is available in the online journal.)

circumbinary disk candidate in our sample of 31 transition disks. A low incidence of circumbinary disk candidates was also found in Papers I and II. The combined sample of 74 transition disks now allows us to derive more robust conclusions on the role multiplicity plays on transition disk systems. As in Paper I, we compare the distribution of binary separations of our sample of transition disk to that of non-transition disk and diskless PMS stars. We draw our sample of non-transition disks (objects with "normal" levels of near-IR excess) and diskless PMS stars from the compilation of multiplicity and *Spitzer* data (for disk identification) presented by Cieza et al. (2009) for over 300 PMS stars in the Taurus, Chameleon I, Ophiuchus, and Corona Australis regions.

As seen in Figure 12, diskless PMS stars tend to have companions at smaller separations than stars with regular, non-transition disks. According to a two-sided Kolmogorov–Smirnov test, there is less than a 10^{-4} probability that the distributions of binary separations of non-transition disks and diskless stars have been drawn from the same parent population. This result can be understood in terms of the effect tidal truncation has on the lifetimes of the circumstellar disks of the individual components of the binary system (Cieza et al. 2009; Kraus et al. 2012). A binary system at the peak of the separation distribution (∼30 AU) is expected to initially have individual disks that are ∼10–15 AU in radius. Given that the viscous timescale is roughly proportional to the size of the disk, such small disks are likely to have accretion lifetimes smaller than the age of the sample and hence they now appear as young diskless stars. In very tight binary systems, the outer disk can survive in the form of a circumbinary disk, with a tidally truncated inner hole with a radius ∼2× the orbital separation (Artymowicz & Lubow 1994). If such close systems were a significant component of the transition disk population, one would expect to find a higher incidence of close binaries in transition disks that in non-transition disks. While our multiplicity census is clearly very incomplete at small separations, our AO observations should be sensitive to an overabundance of companions in the 10–30 AU range that could in principle be responsible for many of the inner holes of our transition disks. However, we find that only ∼4% (3/74) of our transition disks have companions in this separation range. Near-IR interferometry (Pott et al. 2010) and aperture masking observations (Kraus et al. 2009) also suggest that the incidence of tight *stellar* companions is rather low in transition objects. We thus conclude that tight stellar companions tend to destroy each other's disk rather quickly. Few close binary systems retain circumbinary disks with transition disk SEDs (e.g., CoKu Tau/4 and FW Tau).

5.2.3. Constraints on Photoevaporation Models

While it is increasingly clear that photoevaporation by the central star plays a fundamental role on the evolution and dissipation of protoplanetary disks, the heating mechanisms and magnitudes of the photoevaporation rates are still a matter of intense debate. In particular, the relative importance of

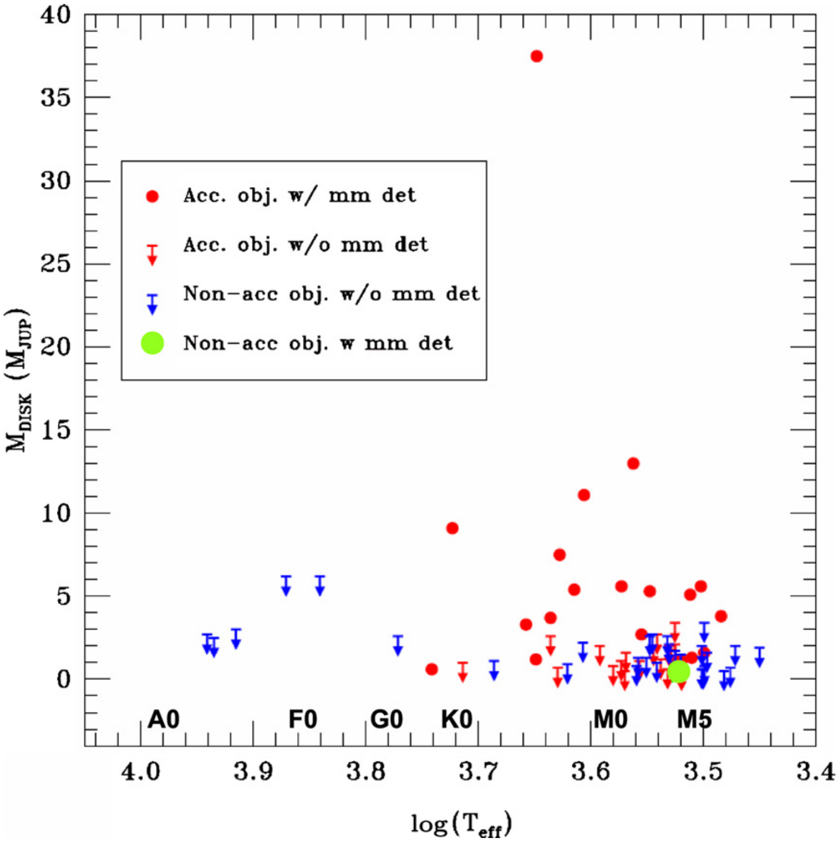

Figure 13. Disk mass as a function of stellar spectral type for our combined sample of transition disks. To avoid overlapping data points, small random offsets have been applied in the X-axis. Only one non-accreting object has been detected at millimeter wavelengths, FW Tau, with an estimated disk mass of 0.4 M_{JUP}. The lack of non-accreting objects with relatively massive outer disks ($\gtrsim$2–5 M_{JUP}) favors photoevaporation models with low evaporation rates ($\sim 10^{-10}$ $M_{\odot}$ yr^{-1}) across a wide range of stellar masses.

(A color version of this figure is available in the online journal.)

far-UV (FUV), EUV, and X-ray photoevaporation is not well understood. All photoevaporation models predict the formation of an inner hole and subsequent inside-out dissipation once mass transport across the disk falls below the photoevaporation rate; however, they strongly disagree on the mass a disk should have at the time the inner hole is formed. EUV-driven photoevaporation models (Alexander et al. 2006) predict low evaporation rates of the order of 10^{-10} $M_{\odot}$ yr^{-1}. As a result, the inner hole forms late on the evolution of the disk, when most of the mass has been depleted (disk mass $\lesssim$1 M_{JUP}) and the accretion rate onto the star has dropped below the 10^{-10} $M_{\odot}$ yr^{-1} level. More recent EUV+X-ray and FUV+X-ray photoevaporation models (Gorti et al. 2009; Owen et al. 2011) predict much higher evaporation rates (10^{-9}–10^{-8} $M_{\odot}$ yr^{-1}) and an earlier formation for the inner hole, when disk masses are $\gtrsim$5 M_{JUP}. These later models allow the presence of accretion in disks with inner holes that have formed through photoevaporation because the accretion rates from the draining of the inner disk become detectable for a significant period of time. However, once the inner disk is drained, accretion must stop as material from the *outer* disk cannot overcome the photoevaporation front. X-ray photoevaporation models thus predict a population of non-accreting objects (i.e., WTTSs) with relatively massive outer disks ($\gtrsim$5 M_{JUP}).

In Paper II, we demonstrated the lack of massive outer disks around low-mass WTTSs, which contradicts the predictions of photoevaporating models with high accretion rates. This result still holds for the new low-mass stars studied herein and seems to extend to higher mass objects. Figure 13 shows the disk masses derived for our combined sample of transition disks. There is only one (sub)millimeter detection at 0.4 M_{JUP} for non-accreting objects (corresponding to FW Tau); the rest are upper limits in the $\sim$0.5 to $\sim$5 M_{JUP} range. Since FW Tau is a circumbinary disk, there is no guarantee that its inner hole is due to photoevaporation. The sample now includes several non-accreting BAFGK stars observed at millimeter wavelengths, but increasing the sample size for this type of object is clearly desirable. An important caveat to Figure 13 is the inherent uncertainty of deriving disk masses from (sub)millimeter photometry, which requires strong assumptions on dust opacities and gas-to-dust mass ratios (Williams & Cieza 2011). If those assumptions are incorrect, they could lead to systematic errors in the determination of disk masses. However, the observed accretion rates of PMS stars provide independent observational constraints that also favor photoevaporation rates significantly lower than 10^{-8} $M_{\odot}$ yr^{-1}. If photoevaporation rates are $\sim 10^{-8}$ $M_{\odot}$ yr^{-1}, then it becomes difficult to explain all the CTTSs without inner holes that have accretion rates less than $\sim 10^{-8}$ $M_{\odot}$ yr^{-1} (Hartmann et al. 1998). Overall, the observational evidence suggests that photoevaporation rates must be small ($\sim 10^{-10}$ $M_{\odot}$ yr^{-1}) and that the photoevaporation front can only overcome accretion when disk masses have fallen below $\lesssim$1 M_{JUP}.

5.2.4. Disk Types as a Function of Stellar Spectral Type and Age

While the samples in Papers I and II were strongly dominated by M-type stars, our current combined sample does contain a

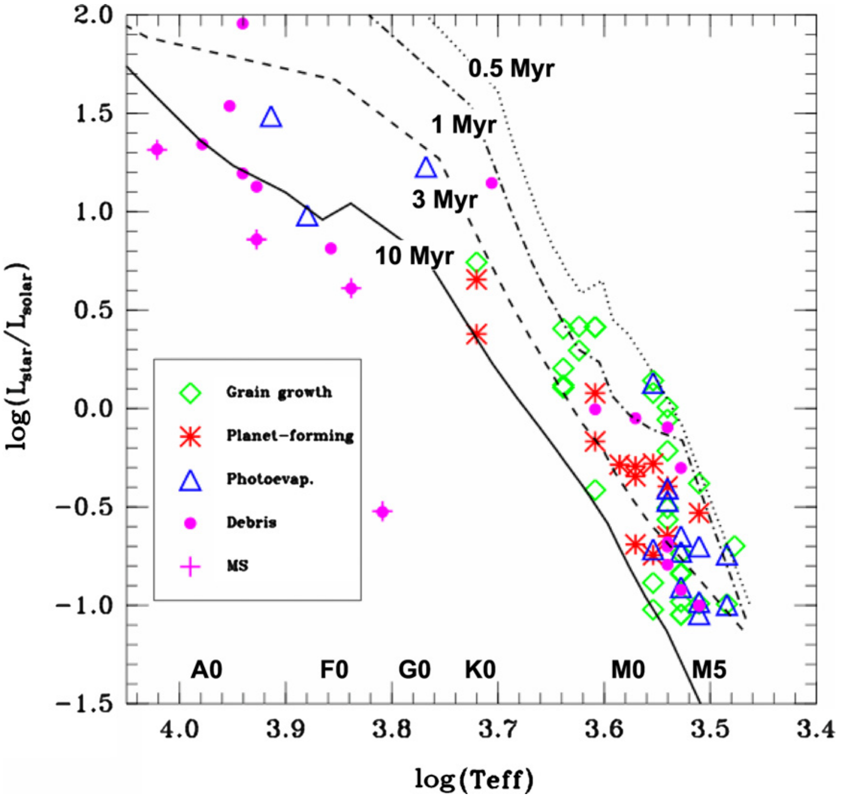

Figure 14. H-R diagram as in Figure 3, but showing the location of each type of disk for the combined sample of disks from Papers I, II, and III. All stars hotter than $\sim 10^{3.76}$ (5754 K, corresponding to a G5 star) have non-accreting disks, either photoevaporating disks or debris disks, consistent with the idea that primordial disks dissipate faster around more massive objects. There is a lack of (giant) planet-forming disk candidates among the youngest stars in the sample. This favors core accretion as the main planet formation mechanism and a 2–3 Myr formation timescale.

(A color version of this figure is available in the online journal.)

Table 4
Disk Types as a Function of Spectral Type for Combined Sample[a]

Spectral Types	Grain-growth-dominated	Giant Planet-forming	Photoevaporating	Debris
All stars	39.2% (29/74)	17.6% (13/74)	20.3% (15/74)	23.0% (17/74)
M-type stars	39.6% (19/48)	16.6% (8/48)	25.0% (12/48)	18.8% (9/48)
K-type stars	58.8% (10/17)	29.4%(5/17)	0.0% (0/17)	11.8% (2/17)
BAFG-type stars	0.0% (0/9)	0.0% (0/9)	33.3% (3/9)	66.6% (6/9)

Note. [a] It includes all transition disks from Papers I–III.

significant number of higher mass BAFGK-type stars. These allow us to investigate whether the incidence of the disk clearing mechanisms depends on stellar mass or luminosity. Figure 14 shows the same H-R diagram as in Figure 3, but now indicating the location of each type of disk. The most striking feature of the diagram is that all nine PMS stars hotter than $\sim 10^{3.76}$ (5754 K, corresponding to a G5 star) have non-accreting disks, either photoevaporating disks or debris disks. This is in agreement with the results from *Spitzer* studies of young stellar clusters and associations showing that primordial disks dissipate faster around higher mass stars (Carpenter et al. 2006; Dahm & Hillenbrand 2007). The four MS stars with debris disks are also hot BAF-type stars. This can be understood considering that debris disks are easier to detect at mid-IR wavelengths around more luminous objects (e.g., Rieke et al. 2005; Hernández et al. 2006; Cieza et al. 2008a). Table 4 shows the occurrence of different types of transition disks for M-type (48 objects), K-type (17 objects), and BAFG-type stars (9 objects) in our combined sample. Since M-type stars are fainter and cooler than higher mass stars, they may present weaker near-IR and/or mid-IR excesses even without grain growth and dust settling effects (Ercolano et al. 2009). However, the fact that we see a *lower* fraction of grain-growth-dominated disk candidates around M-type stars than around K-type stars suggests that we are not significantly overestimating the fraction of M-type stars in this category. Detailed modeling of individual objects is still needed to confirm the nature of some of these grain-growth-dominated disks, especially the ones around very late M-type stars with modest decrements of IR emission. However, it is clear that grain growth and dust settling play a fundamental role on the evolution of circumstellar disks. The grain-growth-dominated disk category accounts for $\gtrsim$40% of all disks around both the M-type stars and K-type stars in our sample.

Currie & Sicilia-Aguilar (2011) recently showed that the percentage of disks in the transition phase increases significantly between ∼1 and ∼8 Myr. The H-R diagram in Figure 14, showing our combined sample, now allows us to investigate how the incidence of different transition disk *types* evolves

Table 5
Disk Types as a Function of Age for Combined Sample[a]

Age	Grain-growth-dominated	Giant Planet-forming	Photoevaporating	Debris
<1 Myr	71.4% (10/14)	0.0% (0/14)	14.3% (2/14)	14.3% (2/14)
1–3 Myr	33.3% (10/30)	26.7% (8/30)	20.0% (6/30)	20.0% (6/30)
>3 Myr	30.0% (9/30)	16.7% (5/30)	23.3% (7/30)	30.0% (9/30)

Note. [a] It includes all transition disks from Papers I–III.

with age. While the stellar ages of individual targets are highly uncertain, the age distribution of each disk category should carry more meaningful information. Table 5 shows the occurrence of different types of transition disks for objects falling above the 1 Myr isochrone (14 targets), between the 1 and 3 Myr isochrones (30 objects), and below the 3 Myr isochrone (30 objects, *not* including the 4 MS star candidates) in our combined sample. Even with our relatively small sample, we find that the incidence of photoevaporating disks and debris disks increases with age, while the fraction of grain-growth-dominated disks decreases with time. These trends are in agreement with the overall evolution of typical protoplanetary disks (Williams & Cieza 2011). Interestingly, the occurrence of plant-forming disk candidates peaks in the 1–3 Myr old age bin and is ~0% for objects above the 1 Myr age isochrone. The lack of planet-forming disks with ages $\lesssim$1 Myr is suggestive, especially considering that the intrinsic age distribution of these objects is most likely to be narrower than that seen in the H-R diagram, where some of the scatter can be attributed to the observational uncertainties in $T_{\rm eff}$ and luminosity. If taken at face value, these results would imply that (1) the inferred giant planets have formed through core accretion (Lissauer 1993) as gravitational instability models (Boss 2000) favor a younger age distribution and (2) core accretion takes 2–3 Myr to form giant planets massive enough to open a gap in the disk. While important caveats remain (we are dealing with planet-forming disk *candidates*, the sample is relatively small, and stellar ages are highly uncertain and model dependent), these results are promising. In the near future, detailed age analyses of larger samples of transition disks with increasingly clear planet formation signatures are likely to provide strong astrophysical constraints on planet formation timescales.

6. SUMMARY AND CONCLUSIONS

As part of an ongoing program aiming to characterize a large number of *Spitzer*-selected transition disks, we have obtained millimeter wavelength photometry, high-resolution optical spectroscopy, and AO near-infrared imaging for a sample of 31 transition objects located in the Perseus, Taurus, and Auriga molecular clouds. We use these ground-based data to estimate disk masses, multiplicity, and accretion rates in order to investigate the mechanisms potentially responsible for their inner holes. We combined disk masses, accretion rates, and multiplicity data with other information, such as SED morphology and fractional disk luminosity, to classify the disks as *strong candidates* for the following categories: grain-growth-dominated disks (seven objects), giant planet-forming disks (six objects), photoevaporating disks (seven objects), debris disks (11 objects), and cicumbinary disks (one object, which was also classified as photoevaporating disk). Each category represents an educated guess, giving all the available data, on the evolutionary status of the disk or the physical process mainly responsible for the reduced levels of near-IR and/or mid-IR excesses characteristic of the objects in our sample. The boundaries between the categories are of course not perfectly defined. For instance, all primordial disks are expected to simultaneously undergo some degree of grain growth, dust settling, and photoevaporation. Similarly, our criterion to distinguish primordial photoevaporating disks from debris disks is based on L_D/L_* instead of on the gas content of their outer disks, which still remains highly unconstrained. The gas dissipation of the outer disk through photoevaporation is believed to mark the rapid transition from the primordial to the debris disk stage (Williams & Cieza 2011). Conclusively establishing the nature of each target will thus require detailed modeling and follow-up observations. Even with the above caveats, the properties of transition disks can provide important clues on different aspects of disk evolution. Combining our sample of 31 transition disks with those from Papers I and II results in a sample of 74 transition disk objects that have been selected, characterized, and classified in a homogenous way. The main conclusions derived from the analysis of this combined high-quality sample can be summarized as follows:

1. Circumstellar disks with reduced levels of near-IR and/or mid-IR excesses in nearby molecular clouds represent a very heterogenous group of objects with a wide range of SED morphologies, disk masses, accretion rates, and fractional disk luminosities. This diversity points toward distinct evolutionary stages and physical processes driving the evolution of each disk.
2. The incidence of objects with signatures of dynamical clearing by recently formed giant planets is significantly lower than the occurrence of giant planets within 20 AU of mature solar-type stars (~5% versus ~20%). The giant planet disk candidates identified in our survey are likely to represent special cases, where multiple massive planets may be present.
3. The incidence of circumbinary disk candidates in our sample of transition objects is low ($\lesssim$10%), implying that tight *stellar* companions tend to erode each other's disk rather quickly.
4. There is a lack of massive disks around non-accreting stars of a wide range of spectral types, which contradicts the predictions of recent photoevaporation models that find very high evaporation rates ($\sim 10^{-8}\ M_\odot$ yr^{-1}). Our results suggest that photoevaporation rates must be small ($\sim 10^{-10}\ M_\odot$ yr^{-1}) and that the photoevaporation front can only overcome accretion when disk masses have fallen below $\lesssim 1\ M_{\rm JUP}$.
5. Debris disks and photoevaporating disk candidates are more common around hotter stars, consistent with the idea that primordial disks dissipate faster around more massive objects.
6. Grain-growth-dominated disks account for $\gtrsim$40% of our sample of transition disks around K- and M-type stars, confirming that grain growth and dust settling play a

major role on the evolution of primordial circumstellar disks.

7. We find a trend in the sense that the incidence of photoevaporating disks and debris disks increases with age, while the fraction of grain-growth-dominated disks decreases with time, which is consistent with disk evolution models.
8. A preliminary analysis of the age distribution of disks with signatures of dynamical clearing by recently formed giant planets reveals a lack of such objects among the youngest stars in the sample. This favors core accretion as the main planet formation mechanism and a 2–3 Myr formation timescale.

Transition objects are invaluable disk evolution and planet formation laboratories. Detailed modeling and follow-up observations of different types of transition disks are highly desirable to further our understanding of key processes such as grain growth and dust settling, photoevaporation, dynamical clearing, and planet formation itself.

We thank the anonymous referee whose comments and suggestions helped us to significantly improve the paper. Support for this work was provided by NASA through the *Sagan* Fellowship Program under an award from Caltech. M.R.S. acknowledges support from FONDECYT (1061199) and Basal CATA PFB 06/09. G.A.R. was supported by ALMA FUND Grant 31070021. M.D.M. was supported by ALMA-Conicyt FUND Grant 31060010. J.P.W. acknowledges support from the National Science Foundation Grant AST08-08144. A.R.M. acknowledges financial support from Fondecyt in the form of grant number 3110049. This work makes use of data obtained with the *Spitzer Space Telescope*, which is operated by JPL/Caltech, under a contract with NASA.

Facilities: Spitzer (IRAC, MIPS), SMA, JCMT (SCUBA-2), Gemini:Gillett (NIRI), and CFHT (Espadons)

REFERENCES

Alexander, R. D., Clarke, C. J., & Pringle, J. E. 2006, MNRAS, 369, 229
Andrews, S. M., & Williams, J. P. 2005, ApJ, 631, 1134
Andrews, S. M., & Williams, J. P. 2007, ApJ, 671, 1800
Andrews, S. M., Wilner, D. J., Espaillat, C., et al. 2011, ApJ, 732, 42
Artymowicz, P., & Lubow, S. H. 1994, ApJ, 421, 651
Boss, A. P. 2000, ApJ, 536, L101
Brown, J. M., Blake, G. A., Dullemond, C. P., et al. 2007, ApJ, 664, L107
Brown, J. M., Blake, G. A., Qi, C., et al. 2009, ApJ, 704, 496
Bryden, G., Beichman, C. A., Trilling, D. E., et al. 2006, ApJ, 636, 1098
Calvet, N., D'Alessio, P., Hartmann, L., et al. 2002, ApJ, 568, 1008
Calvet, N., D'Alessio, P., Watson, D. M., et al. 2005, ApJ, 630, L185
Cargile, P. A., James, D. J., & Jeffries, R. D. 2010, ApJ, 725, L111
Carpenter, J. M., Mamajek, E. E., Hillenbrand, L. A., & Meyer, M. R. 2006, ApJ, 651, L49
Cieza, L., Padgett, D. L., Stapelfeldt, K. R., et al. 2007, ApJ, 667, 308
Cieza, L. A., Cochran, W. D., & Augereau, J.-C. 2008a, ApJ, 679, 720
Cieza, L. A., Padgett, D. L., Allen, L. E., et al. 2009, ApJ, 696, L84
Cieza, L. A., Schreiber, M. R., Romero, G. A., et al. 2010, ApJ, 712, 925
Cieza, L. A., Swift, J. J., Mathews, G. S., & Williams, J. P. 2008b, ApJ, 686, L115
Cumming, A., Butler, R. P., Marcy, G. W., et al. 2008, PASP, 120, 531
Currie, T., Lada, C. J., Plavchan, P., et al. 2009, ApJ, 698, 1
Currie, T., & Sicilia-Aguilar, A. 2011, ApJ, 732, 24
Dahm, S. E., & Hillenbrand, L. A. 2007, AJ, 133, 2072
D'Alessio, P., Calvet, N., Hartmann, L., Franco-Hernández, R., & Servín, H. 2006, ApJ, 638, 314
Dodson-Robinson, S. E., & Salyk, C. 2011, ApJ, 738, 131
Duchêne, G., Bouvier, J., & Simon, T. 1999, A&A, 343, 831
Dullemond, C. P., & Dominik, C. 2004, A&A, 421, 1075
Dullemond, C. P., & Dominik, C. 2005, A&A, 434, 971
Dullemond, C. P., Hollenbach, D., Kamp, I., & D'Alessio, P. 2007, in Protostars and Planets V, ed. B. Reipurth, D. Jewitt, & K. Keil (Tucson, AZ: Univ. Arizona Press), 555
Duquennoy, A., & Mayor, M. 1991, A&A, 248, 485
Ercolano, B., Clarke, C. J., & Robitaille, T. P. 2009, MNRAS, 394, L141
Erickson, K. L., Wilking, B. A., Meyer, M. R., Robinson, J. G., & Stephenson, L. N. 2011, AJ, 142, 140
Espaillat, C., Calvet, N., D'Alessio, P., et al. 2007, ApJ, 670, L135
Espaillat, C., Furlan, E., D'Alessio, P., et al. 2011, ApJ, 728, 49
Espaillat, C., Ingleby, L., Hernández, J., et al. 2012, ApJ, 747, 103
Evans, N., Calvet, N., Cieza, L., et al. 2009, arXiv:0901.1691
Fiorucci, M., & Munari, U. 2003, A&A, 401, 781
Furlan, E., Hartmann, L., Calvet, N., et al. 2006, ApJS, 165, 568
Ghez, A. M., Neugebauer, G., & Matthews, K. 1993, AJ, 106, 2005
Gorti, U., Dullemond, C. P., & Hollenbach, D. 2009, ApJ, 705, 1237
Hartmann, L., Calvet, N., Gullbring, E., & D'Alessio, P. 1998, ApJ, 495, 385
Harvey, P., Merín, B., Huard, T. L., et al. 2007, ApJ, 663, 1149
Hauschildt, P. H., Allard, F., & Baron, E. 1999, ApJ, 512, 377
Heiderman, A., Evans, N. J., II, Allen, L. E., Huard, T., & Heyer, M. 2010, ApJ, 723, 1019
Herbig, G. H. 1998, ApJ, 497, 736
Hernández, J., Briceño, C., Calvet, N., et al. 2006, ApJ, 652, 472
Ho, P. T. P., Moran, J. M., & Lo, K. Y. 2004, ApJ, 616, L1
Holland, W., MacIntosh, M., Fairley, A., et al. 2006, Proc. SPIE, 6275, 45
Huélamo, N., Lacour, S., Tuthill, P., et al. 2011, A&A, 528, L7
Hughes, A. M., Andrews, S. M., Espaillat, C., et al. 2009, ApJ, 698, 131
Hughes, A. M., Wilner, D. J., Calvet, N., et al. 2007, ApJ, 664, 536
Hughes, J., Hartigan, P., Krautter, J., & Kelemen, J. 1994, AJ, 108, 1071
Ireland, M. J., & Kraus, A. L. 2008, ApJ, 678, L59
Jayawardhana, R., Mohanty, S., & Basri, G. 2003, ApJ, 592, 282
Jørgensen, J. K., Harvey, P. M., Evans, N. J., II, et al. 2006, ApJ, 645, 1246
Kenyon, S. J., Gómez, M., & Whitney, B. A. 2008, Handbook of Star Forming Regions, Vol. 1, ed. B. Reipurth (The Northern Sky ASP Monograph, Vol. 4; San Francisco, CA: ASP), 405
Kenyon, S. J., & Hartmann, L. 1995, ApJS, 101, 117
Konopacky, Q. M., Ghez, A. M., Rice, E. L., & Duchêne, G. 2007, ApJ, 663, 394
Kraus, A. L., & Ireland, M. J. 2012, ApJ, 745, 5
Kraus, A. L., Ireland, M. J., Hillenbrand, L. A., & Martinache, F. 2012, ApJ, 745, 19
Kraus, A. L., Ireland, M. J., Martinache, F., & Lloyd, J. P. 2009, in AIP Conf. Proc. 1094, Cool Stars, Stellar Systems and the Sun, ed. E. Stempels (Melville, NY: AIP), 453
Lada, C. J., Muench, A. A., Luhman, K. L., et al. 2006, AJ, 131, 1574
Leinert, C., Zinnecker, H., Weitzel, N., et al. 1993, A&A, 278, 129
Lissauer, J. J. 1993, ARA&A, 31, 129
Lubow, S. H., & D'Angelo, G. 2006, ApJ, 641, 526
Luhman, K. L., Allen, P. R., Espaillat, C., Hartmann, L., & Calvet, N. 2010, ApJS, 186, 111
Luhman, K. L., Stauffer, J. R., Muench, A. A., et al. 2003, ApJ, 593, 1093
Merín, B., Brown, J. M., Oliveira, I., et al. 2010, ApJ, 718, 1200
Monet, D. G., Levine, S. E., Canzian, B., et al. 2003, AJ, 125, 984
Montes, D. 1998, Ap&SS, 263, 275
Montes, D., Ramsey, L. W., & Welty, A. D. 1999, ApJS, 123, 283
Muzerolle, J., Allen, L. E., Megeath, S. T., Hernández, J., & Gutermuth, R. A. 2010, ApJ, 708, 1107
Muzerolle, J., Hillenbrand, L., Calvet, N., Briceño, C., & Hartmann, L. 2003, ApJ, 592, 266
Najita, J. R., Strom, S. E., & Muzerolle, J. 2007, MNRAS, 378, 369
Natta, A., Testi, L., Muzerolle, J., et al. 2004, A&A, 424, 603
Nguyen, D. C., Scholz, A., van Kerkwijk, M. H., Jayawardhana, R., & Brandeker, A. 2009, ApJ, 694, L153
Oliveira, I., Mern, B., Pontoppidan, K. M., et al. 2009, ApJ, 691, 672
Owen, J. E., Ercolano, B., & Clarke, C. J. 2011, MNRAS, 412, 13
Padgett, D. L. 1996, ApJ, 471, 847
Padgett, D. L., Cieza, L., Stapelfeldt, K. R., et al. 2006, ApJ, 645, 1283
Padgett, D. L., Rebull, L. M., Stapelfeldt, K. R., et al. 2008, ApJ, 672, 1013
Pott, J.-U., Perrin, M. D., Furlan, E., et al. 2010, ApJ, 710, 265
Rebull, L. M., Padgett, D. L., McCabe, C.-E., et al. 2010, ApJS, 186, 259
Rebull, L. M., Stapelfeldt, K. R., Evans, N. J., II, et al. 2007, ApJS, 171, 447
Rieke, G. H., Su, K. Y. L., Stansberry, J. A., et al. 2005, ApJ, 620, 1010
Romero, G. A., Schreiber, M. R., Cieza, L. A., et al. 2012, ApJ, 749, 79

Sicilia-Aguilar, A., Hartmann, L. W., Fürész, G., et al. 2006, AJ, 132, 2135
Siess, L., Dufour, E., & Forestini, M. 2000, A&A, 358, 593
Simon, M., Ghez, A. M., Leinert, Ch., et al. 1995, ApJ, 443, 625
Soubiran, C., Katz, D., & Cayrel, R. 1998, A&AS, 133, 221
Wahhaj, Z., Cieza, L., Koerner, D. W., et al. 2010, ApJ, 724, 835
White, R. J., & Basri, G. 2003, ApJ, 582, 1109
Wilking, B. A., Meyer, M. R., Robinson, J. G., & Greene, T. P. 2005, AJ, 130, 1733
Williams, J. P., & Cieza, L. A. 2011, ARA&A, 49, 67
Wyatt, M. C. 2008, ARA&A, 46, 339
Zhu, Z., Nelson, R. P., Hartmann, L., Espaillat, C., & Calvet, N. 2011, ApJ, 729, 47